POLYTECHNIQUE MONTRÉAL
affiliée à l'Université de Montréal

Linear Stability Analysis of Fluid-Structure Problems Using Time-Linearized Coupled Formulations

ALEXANDRE COUTURE
Département de génie mecanique

Mémoire présenté en vue de l'obtention du diplôme de *Maîtrise ès sciences appliquées*
Génie mécanique

Avril 2020

POLYTECHNIQUE MONTRÉAL
affiliée à l'Université de Montréal

Ce mémoire intitulé :

Linear Stability Analysis of Fluid-Structure Problems Using Time-Linearized Coupled Formulations

présenté par **Alexandre COUTURE**
en vue de l'obtention du diplôme de *Maîtrise ès sciences appliquées*
a été dûment accepté par le jury d'examen constitué de :

André GARON, président
Frédérick GOSSELIN, membre et directeur de recherche
Étienne STÉPHANE, membre et codirecteur de recherche
David VIDAL, membre

ACKNOWLEDGEMENTS

Je tiens principalement à remercier mon directeur de recherche, Frédérick Gosselin. Sa capacité à exposer clairement et simplement ses idées et ses vastes connaissances m'ont définitivement permis de surmonter les innombrables défis auxquels j'ai fait face. Son écoute et sa patience ont aussi été des éléments clés pour me permettre de passer au travers de ma maîtrise. Je remercie aussi mon codirecteur, Stéphane Étienne, qui a toujours su mettre en perspective ma recherche, apporter les bons questionnements et, du fait même, apporter de nouvelle idée à mon projet de recherche.

Je me dois aussi de remercier le Conseil de recherches en sciences naturelles et en génie du Canada (CRSNG), le Fonds de recherche du Québec - Nature (FRQNT) et l'Institut de l'énergie Trottier (IET) pour leur soutien financier vital à la réalisation de ce projet. Leurs subventions m'ont permis d'étudier un sujet de recherche très exploratoire et m'ont donné une grande liberté quant à l'orientation précise de mes travaux.

Je désire également remercier quelques personnes du LM2, principalement Max Louyot, sans qui la solitude intrinsèque à un tel projet de recherche aurait été insurmontable.

Finalement, je veux remercier ma famille et tout particulièrement mes parents pour leur support infaillible tout au long de mes études, merci.

RÉSUMÉ

Les turbines hydroélectriques sont maintenant plus souvent utilisées dans des conditions hors conception et connaissent davantage de cycles de démarrage et d'arrêt en raison de la croissance des sources d'énergie renouvelables et imprévisibles comme l'éolien et le solaire. Ces conditions d'utilisation sont sujettes à des vibrations induites par l'écoulement qui peuvent être problématiques pour la durée de vie en fatigue des turbines hydrauliques. Pour prévenir les dommages causés par ces vibrations, les propriétés vibratoires d'une turbine doivent être bien comprises. L'évaluation numérique des facteurs d'amortissement et de rigidité hydrodynamiques est donc de la plus haute importance, mais elle pose un problème car elle nécessite la simulation des phénomènes complexes d'interactions structure-fluide.

À cette fin, deux méthodes numériques sont développées pour modéliser efficacement les propriétés de stabilité dynamique des problèmes d'interactions fluide-stucture. Les deux méthodes reposent sur la linéarisation temporelle des équations solides et fluides. La première méthode utilise un écoulement potentiel et la seconde utilise les équations de Navier-Stokes pour représenter le fluide. Pour les deux méthodes, le problème d'équations aux dérivées partielles résultant de la combinaison des équations solides, fluides et frontières est discrétisé dans le domaine fréquentiel à l'aide de la méthode des éléments finis. La résolution du problème de valeur propre qui en résulte donne la fréquence et le taux de croissance des différents modes du système couplé. Pour obtenir les propriétés de stabilité des systèmes couplés fluide-structure, des méthodes d'identification et de suivi des modes sont développées pour permettre des analyses paramétriques efficaces. Les deux méthodes sont testées sur des cas simples de plaques en porte-à-faux bidimensionnelles et comparées aux résultats existants. La première méthode, basée sur un écoulement potentiel, s'avère reproduire les résultats de référence que dans certains cas bien particuliers en raison d'un problème dans la représentation du sillage. La seconde méthode, basée sur les équations de Navier-Stokes, montre une meilleure concordance avec les résultats de référence et un coût de calcul beaucoup plus faible que les méthodes conventionnelles.

ABSTRACT

Hydroelectric turbines are now more often used in off-design conditions and experience more start-stop cycles because of the growth of renewable but unpredictable energy sources. These conditions are prone to flow-induced vibrations that can be problematic for the fatigue life of turbine runners. To prevent damage from such vibrations, the vibratory properties of a turbine must be well understood. Numerically evaluating hydrodynamic damping and stiffness factors is thus of the upmost importance but it poses a problem as it requires the simulation of complex fluid-structure phenomena.

To that end, two numerical methods are developed to efficiently model the dynamic stability properties of complex fluid-structure problems. Both methods rely on the time linearization of coupled solid and fluid equations. The first method uses a potential flow and the second uses Navier-Stokes equations to represent the fluid. For both methods, the partial differential equations problem resulting from combining the solid, fluid and boundary equations is discretized in the frequency domain using the finite element method. Solving the resulting eigenvalue problem yields the frequency and growth rate of the coupled system. To obtain the stability properties of the fluid-structure interaction systems, mode identification and tracking methods are developed to allow for efficient parameter analyses. Both methods are tested on simple two-dimensional cantilever plate cases and compared to existing results. The first method, based on a potential flow, is found to have limited agreement to reference results due to strong limitations in the representation of the wake. The second method, based on the Navier-Stokes equations, shows better agreement with reference results and a much smaller computational cost than conventional methods.

TABLE OF CONTENTS

LIST OF FIGURES

CHAPTER 1 INTRODUCTION

The study of fluid-structure interaction (FSI) is essential for the proper understanding of a large variety of engineering problems: from the flutter instability of airplanes wings to the vortex-induced vibrations (VIV) of offshore drilling risers. Both these types of problems, flutter and VIVs, arise from the coupling of unsteady fluid-dynamic, inertial and elastic forces [4]. Being able to predict the onset of instability of these systems, and prevent it, is of the utmost importance.

Various numerical methods have been developed to evaluate the stability of FSI problems, depending on their properties [5], but even after decades of research, the simulation of many FSI problems remains a challenge [6]. Advanced methods coupling non-linear fluid and solid equations with time-marching algorithms are now capable of numerically reproducing FSI phenomenons, but they remain computationally intensive. Thus, their use for complex cases such as the oscillations of hydroelectric turbine runners remains limited. Generally, for such problems, various models or numerical simplifications are used [7].

Efficiently obtaining the vibratory properties of hydraulic turbine runners is the problem that inspired the methods presented in this thesis. The goal is to develop a method capable of quickly evaluating the added mass and damping effect of hydroelectric runners. These parameters are important for the study of the fatigue life of this equipment. It was studied both experimentally [8, 9] and numerically [10, 11], but the numerical methods employed are generally too computationally intensive to allow for large parameter sweep and shape optimization.

The present thesis describes two numerical methods aimed at efficiently obtaining the linear stability limits and properties of complex FSI problems, such as hydroelectric turbine runners. More specifically, methods based on time-linearisation and the coupling of fluid and solid equations are presented. First, the linear elasticity equation is combined with a potential flow with dynamic and kinematic coupling boundary conditions. The problem is transformed into an eigenvalue problem by using the small perturbation hypothesis and a finite element formulation. The development and testing of this potential method is presented in chapter 2. Secondly, the solid elasticity equations are combined with Navier-Stokes equations again using small perturbations and finite elements. The development and testing of the Navier-Stokes method is the subject of chapter 3. The added complexity of the fluid representation in this second method requires particular attention in the coupling boundary conditions and the treatment of the results. Both methods are tested with simple two-dimensional geometries

that were the subject of previous studies [1, 3]. In developing the potential method, an important limitation was found in the applicability of the wake boundary condition. This led to the development of the Navier-Stokes method which shows better agreement with results obtained with time-marching non-linear methods.

1.1 Motivation

In many electricity markets around the world, there is an increasing proportion of the total energy production that is provided by wind and solar at the expense of classic thermal or hydroelectric power plants [12]. The power provided by these renewable sources is difficult to predict precisely beyond a few days or hours and often does not match the daily variation of demand. This mismatch has increased the need to utilize the conventional and predictable sources to compensate for these variations. Multiple other solutions such as large batteries, compressed air or pumped hydroelectric storage could alleviate this problem [13], but, as those solutions are not widely implemented, grid operators still require more flexibility from the existing installations. Thus, in markets where hydroelectricity dominates, the increasing importance of renewable energy sources is modifying the usage of hydroelectric installations [14].

Historically, hydroelectric turbines were designed to provide base power to the grid, but, with the growth of intermittent renewable sources, they are now increasingly used as grid regulators [15]. Unfortunately, frequent start-stop cycle, large load variations and operation outside of the peak efficiency point can have adverse effects on the lifetime and maintenance requirements of turbine runners [16].

Load variations and startups can induce transitory flow instabilities and operation far from the design conditions and spin-no-load conditions can cause constant flow instabilities. At the source of these instabilities are multiple phenomena. In Francis turbines, one of the main types of hydraulic turbines, there exists, among other, five main sources of flow-induced vibrations: rotor-stator interaction, Von Karman vortices, turbulence, cavitation and draft tube vortex rope [17].

These instability phenomena are each a research subject of their own. They operate in multiple frequency ranges and they may all be the source of problematic runner vibrations. Vibrations of the turbine runner can over time induce and encourage the propagation of cracks through fatigue of the turbine runners' material [18]. Hence, understanding the vibratory properties of operating turbine runners, such as the added mass, hydrodynamic damping and

stiffness caused by the water flow, is necessary to predict the lifetime of current runners and prevent excessive vibrations for new installations.

The added mass parameter can be obtained experimentally [19] or through well established numerical simulations combining elastic and acoustic equations for the runner and surrounding water respectively [20]. On the other hand, added damping and stiffness are harder to estimate numerically. Unlike, added mass, they are strongly related to the flow velocity, and thus, requires more complex fluid considerations [8, 11, 21].

1.2 Context

The study of the linear stability of structures immersed in a fluid flow was initially studied in the context of aeroelasticity to understand and prevent aircraft wing flutter [22]. In aeroelasticity, multiple simplifying assumptions are generally taken on the structure and the flow; the wing is generally modeled using a rigid airfoil with few degrees of freedom and the high Reynolds flow around the wing is considered irrotational and inviscid, and is thus modeled with potential equations. For wing flutter, the time scale of the fluid motions is much smaller than that of the solid's motions; static aerodynamic coefficients can thus be used to determine the aerodynamic forces [4]. This quasi-steady approach can accurately predict the onset of instability of aircraft wing flutter but this method is not generalizable to fluid-structure phenomena where the fluid and solid times scales are closer to each other. The aeroelasticity method is also difficult to generalize to cases with more complex fluid flows. As such, this method is hardly applicable to hydraulic turbines.

To allow the simulation of more complex fluid-structure phenomena, numerical models closer to the physical realities they try to represent were developed. Many simulation methods that take fewer assumptions about the fluid and solid were developed using various numerical schemes and coupling mechanism. [23]. More precisely, methods combining Navier-Stokes equations and non-linear solid equations through the Arbitrary-Langrangian-Eulerian (ALE) formulation allow for the time marching simulations of complex FSI cases [24]. Some methods use a partitioned approach by solving the fluid and solid parts sequentially and ensure the coupling between both domains is achieved using multiple iterations [25, 26], while other use monolithic approaches where both domains are solved simultaneously [27]. The multiple methods presented in the literature differ from each other on numerical and implementation details such as the time-stepping scheme, the discretization methods of either domain, the coupling method and grid adjustment methods among many others. [23]. Although these methods have seen great improvements over the years, they still remain very computationally

intensive. This prohibits their use for parameter analysis and optimization algorithms which require the simulation of vast quantities of configurations.

To reduce the computational cost of simulating complex FSI problems, multiple methods, such as reduced order models or time-linearized methods, were developed. For FSI methods, reduced order models generally refer to the proper orthogonal decomposition method [28]. The number of degrees of freedom of a problem is greatly reduced by assuming the movement of both domains to be a combination of multiple orthogonal modes obtained through *a posteriori* analysis of complete time simulations [29, 30]. While reduced order models allow faster simulations than high fidelity methods, they generally cannot be applied to problems including large solid displacements.

Just as reduced order models, the methods presented in this thesis are also not applicable to large solid displacement, but they allow for the rapid evaluation of the stability limits of some FSI problems. Both are based on the time-linearized approach through which we assume small perturbations for both the fluid and solid variables around a base configuration which is computed beforehand. The kinematic coupling between the fluid domain is treated using a transpiration method based on the work by Lighthill [31]. The dynamic boundary condition is derived by equating the boundary stress of each domain and properly applying the small perturbation hypothesis.

The first method, which uses a potential flow and is presented in chapter 2, is an extension of the added-mass formulation widely used for structures immersed in a static fluid [32]. As its name indicates, this method allows the easy evaluation of the added-mass caused by the presence of the fluid. It is used in various fields such as bio-mechanics [33] and hydraulic turbines [34]. By adding a base flow to this method, through *a priori* solving of a simple potential flow, we introduce convection terms to the formulation and particular attention must be given to the fluid-structure boundary conditions.

The results of the potential method were compared to those of Guo and Paidoussis [1]. This paper studies the linear stability of rectangular plates with free side-edges in a two-dimensional inviscid channel flow. It assumes the one-dimensional motion of an elastic plate and couples it with an inviscid flow composed of a base plug flow and a perturbation potential flow. The Galerkin method and the Fourier transform technique are used to solve the equations and obtain the complex eigenvalues of the coupled modes. The evolution of the two modes with the smallest real parts is presented for various boundary condition of the plate such as fixed-fixed and fixed-free. One of the fundamental differences between their method and the potential method is in the consideration of the wake. This difference is found to be

problematic to the applicability of the potential method and motivated the development of the Navier-Stokes method.

The second method, which uses the Navier-Stokes equations and is presented in chapter 3, is based on the method presented by Fernandez and Le Tallec in [35, 36]. They propose the linearization of the fluid-structure ALE equations into a Eulerian formulation and they derive Eulerian-based boundary conditions for velocity and stress at the fluid-structure interface. The manner in which their model is derived and presented is different than in the present thesis and their test case is also different. The work of Fernandez and Le Tallec also inspired a recent paper by Pfister et al. [2] which arrives at a numerical model similar to ours, but still fundamentally different.

Similarly to the Navier-Stokes method presented here, Pfister et al. also couple the Navier-Stokes equations with the linear elasticity equation, but to couple both domain, they introduce an extension displacement field that is defined in the fluid domain, close to the structure. As we do not implement such a field, the treatment on the fluid-structure boundary conditions is different. Also, they implemented a complete steady FSI solver and they can thus account for the deformation and stress caused by the base flow. Pfister et al. tested their method with three test cases: an elastic plate clamped behind a fixed cylinder in a two-dimensional flow, a cantilever elastic plate clamped at the trailing edge of an infinite rigid plate in a two-dimensional channel flow and a three-dimensional plate perpendicular to a flow.

The Navier-Stokes method presented here is tested with the same case of a cantilever elastic plate clamped at the trailing edge of an infinite rigid plate as in the paper of Pfister et al. This test case was also studied by Cisonni et al. [3] with a time-marching marching algorithm coupling Navier-Stokes equations with a one-dimensional elastic beam model. This more traditional method was used to execute a parameter analysis on the stability of the plate, but it required approximately 150,000 CPU hours on modern hardware to compute around 120,000 simulations of this relatively simple two-dimensional test case. This shows the relevance of developing a quicker method to evaluate the stability of complex coupled fluid-structure systems.

1.3 Objectives

The general objective of the present thesis is to study numerical methods for simulations of fluid-structure interaction problems based on frequency domain formulations. The methods are developed to efficiently predict the onset of instability and to evaluate the added stiff-

ness, damping and mass parameters of structures subject to fluid flows. The methods are implemented in ways that allow their generalization to complex geometries such as hydraulic turbines.

The fundamental idea behind both methods presented in this thesis is the combination of well-established fluid and structure formulations, coupling methods and linearization methods, but very few similar fluid-structure simulation methods have been studied in the literature. Thus, the first specific objective is to present a detailed development of the methods' formulation going from the fundamental equations to the tools used for their implementation. Particular attention is given to the development and integration of the fluid-structure interface boundary conditions.

The second objective is to validate the proposed methods by applying them to reference cases for which data already exists in the literature. Both the potential and Navier-Stokes methods are applied to the problem of a plate in a channel axial flow, albeit with different conditions considering the first method uses an inviscid fluid and the second is developed for low Reynolds flows.

The first method, based on a potential flow, is developed to benefit from the simplicity of the potential formulation and its capacity to approximate high Reynolds flows, such as those in hydraulic turbines. Unfortunately, the additional boundary condition necessary to account for the wake proved to be problematic with our formulation. This led to the development of the second method, based on the Navier-Stokes equations.

This second method is developed to get closer to the actual physics of the problem at hand. It is a first step towards a method capable of rapidly predicting the stability of complex high Reynolds FSI problems such as hydraulic turbines.

CHAPTER 2 Potential method

In trying to develop a numerical method to quickly evaluate the dynamic stability of flexible structures subject to heavy fluid flows, we first develop a method based on combining a linear elastic solid domain with an inviscid and incompressible fluid represented with a velocity potential. This method, herein referred to as the potential method, is based on the hypothesis of small perturbations of the solid displacement and fluid velocity. We then assume harmonic forms for both solid and fluid variables, which yields an eigenvalue problem that is solved using the finite element method.

We decided to first apply the potential method to the case of a simple plate in axial flow, i.e. the flag problem. More specifically, we considered plates with various leading and trailing edge boundary conditions in a two-dimensional inviscid channel flow. This base case was selected to allow the comparison of our results with those from Guo and Paidoussis. [1]. This paper solves the same problem but neglects the thickness of the plate and their method is not generalizable to complex geometries.

In this chapter, the discretized eigenvalue problem is derived from the linear elasticity and Euler equations. Next, meshing and software implementation is detailed. Finally, the stability behavior obtained from the potential method is compared to the reference results from Guo and Paidoussis.

2.1 Method details

2.1.1 Governing equations

The purpose of this method is to predict the onset of instability for structures with complex geometries. We are not trying to simulate the inherently non-linear behavior of such structures when they are unstable; we are only interested in the linear displacements of the structures around a static equilibrium position that herein is described as the base configuration. The base configuration results from the deformation of the structure due to the base flow. It is important to differentiate it from the reference configuration which corresponds to the configuration of the structure without any external forces applied. Variables and operators expressed in the reference configuration are denoted with the hat symbol.

To study the equilibrium around the base configuration, we use the hypothesis of small perturbations for the vibration of the structural domain. Consequently, the structures in this method are represented with linear elastic theory. We only consider isotropic material

for validation and because most of the structures of interest are metallic. Thus, the field of solid displacement $\hat{\boldsymbol{d}}_{\boldsymbol{s}}$, defined on the solid domain Ω_s, respects:

$$\rho_s \frac{\partial^2 \hat{\boldsymbol{d}}_{\boldsymbol{s}}}{\partial t^2} - \nabla \cdot \hat{\boldsymbol{\sigma}}(\hat{\boldsymbol{d}}_{\boldsymbol{s}}) - \hat{\boldsymbol{F}} = 0, \tag{2.1}$$

where t is the time, ρ_s is the solid density, $\hat{\boldsymbol{\sigma}}(\hat{\boldsymbol{d}}_{\boldsymbol{s}})$ is the Cauchy stress tensor and $\hat{\boldsymbol{F}}$ is the external volumetric force vector. For our test case, we do not impose any external volumetric force, which would generally be used to include gravity. Using Hooke's law, we can write the stress tensor as:

$$\hat{\boldsymbol{\sigma}}(\hat{\boldsymbol{d}}_{\boldsymbol{s}}) = 2\mu\hat{\boldsymbol{\epsilon}}(\hat{\boldsymbol{d}}_{\boldsymbol{s}}) + \lambda tr[\hat{\boldsymbol{\epsilon}}(\hat{\boldsymbol{d}}_{\boldsymbol{s}})]\boldsymbol{I},$$

where $\boldsymbol{\epsilon}(\boldsymbol{d}_{\boldsymbol{s}})$ is the infinitesimal strain tensor. The first and second Lamé coefficients, λ and μ respectively, are defined as:

$$\lambda = \frac{E_s \nu_s}{(1+\nu_s)(1-2\nu_s)}, \quad \mu = \frac{E_s}{2(1+\nu_s)},$$

where E_s is the Young's modulus and ν_s is the Poisson ratio.

To implement our method with the small perturbation hypothesis, the solid and fluid variables need to be defined around a base state. This base state configuration is computed before the stability analysis is completed. In equation (2.1), $\hat{\boldsymbol{d}}_{\boldsymbol{s}}$ describes the total solid displacement from the reference configuration that may be different to the base configuration. For our stability analysis, we separate the variables into their 0th order term $\hat{\boldsymbol{d}}_{\boldsymbol{s,b}}$ defined around the reference configuration and 1st order small perturbation term $\boldsymbol{d}_{\boldsymbol{s}}$ defined around the deformed base configuration:

$$\hat{\boldsymbol{d}}_{\boldsymbol{s}} = \hat{\boldsymbol{d}}_{\boldsymbol{s,b}}(\hat{\boldsymbol{X}}) + \boldsymbol{d}_{\boldsymbol{s}}(\boldsymbol{X}'_{\boldsymbol{t}}, t) + \mathcal{O}(\epsilon^2), \tag{2.2}$$

where t is time, $\hat{\boldsymbol{X}}$ is the position vector from the reference configuration and $\boldsymbol{X}'_{\boldsymbol{t}}$ is the position vector from the deformed base position. The presence of the subscript t on $\boldsymbol{X}'_{\boldsymbol{t}}$ expresses the fact that the solid small displacement variable $\boldsymbol{d}_{\boldsymbol{s}}$ uses a Lagrangian field specification. This distinction is important because the small displacement variables in the fluid domain are defined using an Eulerian specification. This difference requires particular attention in the imposition of the boundary conditions at the fluid-structure interface. Using (2.2) in

(2.1), we get the 0th-order and 1st-order equations:

$$\nabla \cdot \hat{\boldsymbol{\sigma}}(\hat{\boldsymbol{d}}_{\boldsymbol{s,b}}) = 0, \tag{2.3}$$

$$\rho_s \frac{\partial^2 \boldsymbol{d_s}}{\partial t^2} - \nabla \cdot \boldsymbol{P}(\boldsymbol{d_s}, \hat{\boldsymbol{d}}_{\boldsymbol{s,b}}) = 0, \tag{2.4}$$

where $\boldsymbol{P}$ is the first Piola-Kirchhoff stress tensor. It allows us to account for the stress in the base configuration. Details on the use of the Piola-Kirchhoff stress tensor are given in the next chapter. As will be described later, we assume, for our test case, that the deformation caused by the base flow is negligible, i.e. $\hat{\boldsymbol{d}}_{\boldsymbol{s,b}} = 0$ and $\hat{\boldsymbol{X}} = \boldsymbol{X'}$. Thus, the 0th-order equation (2.3) is not used in the resolution of our test case and the 1st-order equation (2.4) comes back to an equation very similar to (2.1):

$$\rho_s \frac{\partial^2 \boldsymbol{d_s}}{\partial t^2} - \nabla \cdot \boldsymbol{\sigma}(\boldsymbol{d_s}) = 0 \text{ on } \Omega_s. \tag{2.5}$$

In the potential method, we assume the fluid to be incompressible, inviscid and irrotational. Although we could start from the potential flow equation, it is still relevant to start from the Euler equations to derive some relations used in the model. Starting with the continuity and momentum equations for an inviscid and incompressible fluid, we get:

$$\nabla \cdot \boldsymbol{U_f} = 0, \tag{2.6}$$

$$\rho_f \Big[\frac{\partial \boldsymbol{U_f}}{\partial t} + (\boldsymbol{U_f} \cdot \nabla)\boldsymbol{U_f} \Big] - \nabla P = 0, \tag{2.7}$$

where ρ_f is the fluid density, $\boldsymbol{U_f}$ is the fluid velocity vector and P is the pressure. Just as for the solid displacement, we decompose the fluid variables into their base and small perturbation components:

$$\boldsymbol{U_f} = \boldsymbol{u_{f,b}}(\boldsymbol{X}) + \boldsymbol{u_f}(\boldsymbol{X'}, t) \tag{2.8}$$

$$P = p_b(\boldsymbol{X}) + p(\boldsymbol{X'}, t). \tag{2.9}$$

By introducing this decomposition into (2.6) and considering the linearity of the gradient operator, we get the following 0th-order and 1st-order equations:

$$\nabla \cdot \hat{\boldsymbol{u}}_{\boldsymbol{f,b}} = 0 \quad \text{and} \quad \nabla \cdot \boldsymbol{u_f} = 0. \tag{2.10}$$

In our test case, described later, we will assume a potential base flow, and thus satisfy the first equation of (2.10). By introducing a velocity potential, defined as:

$$\boldsymbol{u_f} = \nabla\phi, \tag{2.11}$$

into the second equation of (2.10), we can define the governing perturbation equation in the fluid domain Ω_f:

$$\Delta\phi = 0 \text{ on } \Omega_f, \tag{2.12}$$

where Δ is the Laplace operator, i.e, $\Delta\phi = \nabla \cdot \nabla\phi$. The momentum equation (2.7) is used to express the pressure as a function of the velocity potential. By introducing (2.8) and (2.9) into (2.7), we get:

$$\rho_f\Big[\frac{\partial \boldsymbol{u_{f,b}} + \boldsymbol{u_f}}{\partial t} + ((\boldsymbol{u_{f,b}} + \boldsymbol{u_f}) \cdot \nabla)(\boldsymbol{u_{f,b}} + \boldsymbol{u_f})\Big] = -\nabla(p_b + p).$$

By developing this last equation, we obtain the 0th-order and 1st-order equations which must be satisfied independently:

$$\rho_f\Big[\frac{\partial \boldsymbol{u_{f,b}}}{\partial t} + (\boldsymbol{u_{f,b}} \cdot \nabla)\boldsymbol{u_{f,b}}\Big] + \nabla p_b = 0,$$

$$\rho_f\Big[\frac{\partial \boldsymbol{u_f}}{\partial t} + (\boldsymbol{u_f} \cdot \nabla)\boldsymbol{u_{f,b}} + (\boldsymbol{u_{f,b}} \cdot \nabla)\boldsymbol{u_f} + (\boldsymbol{u_f} \cdot \nabla)\boldsymbol{u_f}\Big] + \nabla p = 0.$$

As will be seen in the next subsection, the base flow of our test case can be approximated to a plug flow, i.e. a constant, thus the term $(\boldsymbol{u_f} \cdot \nabla)\boldsymbol{u_{f,b}}$ can be neglected. By eliminating it and the second order term $(\boldsymbol{u_f} \cdot \nabla)\boldsymbol{u_f}$ in the last equation, we are left with:

$$\rho_f\Big[\frac{\partial \boldsymbol{u_f}}{\partial t} + (\boldsymbol{u_{f,b}} \cdot \nabla)\boldsymbol{u_f}\Big] + \nabla p = 0. \tag{2.13}$$

By introducing the definition (2.11), we can express the fluid pressure as a function of the velocity potential ϕ:

$$p = -\rho_f[\frac{\partial\phi}{\partial t} + (\boldsymbol{u_{f,b}} \cdot \nabla)\phi]. \tag{2.14}$$

2.1.2 Test case description

To test the potential method, we study the stability of plates in a two-dimensional channel flow. Figure 2.1 shows details of the geometry of our test case: the different domains and boundaries and the definition of different dimensional parameters. This test case is similar to

the one proposed and analyzed in Guo and Paidoussis [1]. Unlike their test case, our plate has a finite thickness. We could have used one-dimensional elements to represent the plate, but such a method would require a considerable idealisation and modeling task. Considering our goal is to create a generalizable method, using a two-dimensional solid domain is necessary. The small discrepancies caused by the presence of the thickness will be studied and it is shown not to be significant in the comparison of our results with those of Guo and Paidoussis.

Our method is solved with dimensional values but the comparison of the results must be done through three non-dimensional numbers: the reduced speed U_R, the mass ratio μ, and the height ratio c. These are defined as:

$$U_R = L\sqrt{\frac{\rho_s h_p}{D}}U, \quad \mu = \frac{\rho_f L}{\rho_s h_p}, \quad c = \frac{h}{L},$$

where D is the plate bending stiffness defined as :

$$D = \frac{E_s h_p^3}{12(1-\nu^2)}.$$

The eigenvalues resulting from our method, ω are dimensionnal but are presented as the dimensionless eigenvalue $\bar{\omega}$ defined as:

$$\bar{\omega} = L^2\sqrt{\frac{\rho_s h_p}{D}}\omega.$$

We focus on clamped-free and clamped-clamped boundary conditions. Dimensional parameters of our model are selected to match the non-dimensional parameters μ and c of Guo and Paidoussis and the parameter sweep over U_R is done by varying the dimensional flow velocity U.

2.1.3 Base flow computation

The potential flow method would generally require solving a coupled fluid-structure problem to obtain the base state $(\boldsymbol{d_{s,b}}, \boldsymbol{u_{f,b}})$ around which the stability analysis is done. For our test case, the extension stiffness is much greater than the bending stiffness because of the small aspect ratio of the plate. Thus, the extension of the plate is negligible and the base configuration geometry is equivalent to the reference configuration geometry. Also, because our base flow is potential, it does not generate drag, and thus, axial loads on the plate.

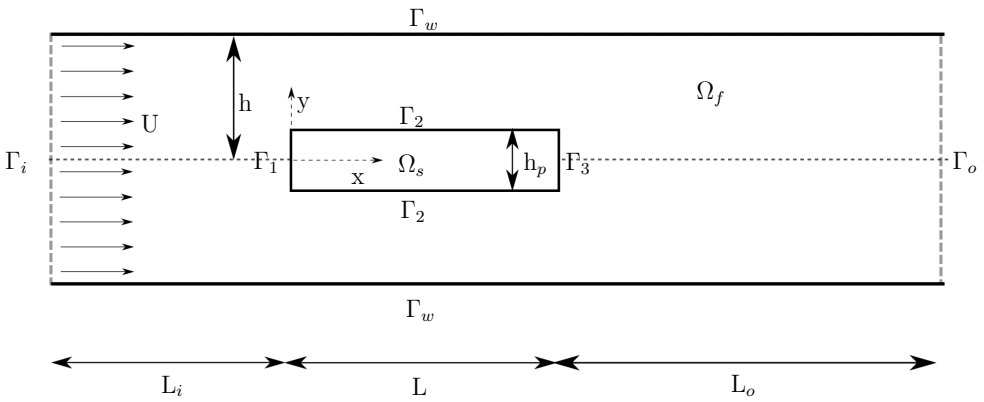

Figure 2.1 Schematic representation of the plate in parallel flow test case for the potential method indicating the domains and boundaries nomenclature and the problem's geometric measurements.

This assumption simplifies the computation of the base configuration to only solving the base flow around the plate. To that end, we take a base velocity potential similar to (2.11) but with the base flow velocity $\boldsymbol{u_{f,b}}$:

$$\boldsymbol{u_{f,b}} = \nabla \phi_b. \tag{2.15}$$

By introducing this potential in the 0th order continuity equation (2.10), we get the governing equation of our base flow:

$$\Delta \phi_b = 0. \tag{2.16}$$

For the test case, non-penetration boundary conditions are applied on the upper and lower walls, and on the plate. On the inlet, a horizontal fluid velocity U is imposed and, on the outlet, a null velocity potential is imposed. The boundary condition for the base flow are thus expressed as:

$$\begin{cases} \frac{\partial \phi_b}{\partial x} = U \quad \text{on } \Gamma_i & (a) \\ \phi_b = 0 \quad \text{on } \Gamma_o & (b) \\ \nabla \phi_b \cdot \boldsymbol{n} = 0 \quad \text{on } \Gamma_w, \Gamma_1, \Gamma_2, \Gamma_3 & (c) \end{cases} \tag{2.17}$$

To solve this equation, we develop its weak form to implement it using finite elements. First, we define the following functional space over which the fluid base velocity potential is defined:

$$\mathcal{P}_b = \{\phi_b \to \mathbb{R} | \phi_b \in \mathcal{H}^1, \phi_b = 0 \text{ on } \Gamma_f^D\},$$

where Γ_f^D are the boundaries where a Dirichlet condition is applied. To develop the weak formulation of (2.16), we must also introduce a test function ψ_b that is also defined over $\mathcal{P}_b$. By multiplying (2.16) by the test function and integrating over the fluid domain, we get :

$$\int_{\Omega_f} \Delta\phi_b \psi_b dV = 0. \tag{2.18}$$

By applying the first Green identity and introducing the boundary conditions (2.17), we get the weak formulation equation governing the base flow of our test case:

$$\int_{\Omega_f} (\nabla\phi_b \cdot \nabla\psi_b) dV - \int_{\Gamma_i} U\psi dS = 0. \tag{2.19}$$

This equation is discretized and solved using the same mesh as in the stability analysis. Details of this mesh are given later. By using (2.15), we can obtain the base flow velocity field $\boldsymbol{u_{f,b}}$ from the solution of (2.19).

2.1.4 Boundary conditions

The fluid-structure boundary requires particular attention because it is at the core of our method. To couple both domains, we impose the impermeability of the boundary with a kinematic condition and the transfer of forces with a dynamic condition.

As mentioned earlier, the solid displacement variable is defined with a Lagrangian specification and the fluid is defined with an Eulerian specification. To make both specifications agree, we use a material derivative of the solid small displacements:

$$\boldsymbol{u_f} \cdot \boldsymbol{n} = \frac{D\boldsymbol{d_s}}{Dt} \cdot \boldsymbol{n} = \frac{\partial \boldsymbol{d_s}}{\partial t} \cdot \boldsymbol{n} + (\boldsymbol{u_{f,b}} \cdot \nabla \boldsymbol{d_s}) \cdot \boldsymbol{n}. \tag{2.20}$$

The normal vector $\boldsymbol{n}$ is defined outward from the solid domain. By introducing (2.11) into (2.20), the kinematic boundary condition becomes:

$$\nabla\phi \cdot \boldsymbol{n} = (\frac{\partial \boldsymbol{d_s}}{\partial t} + \boldsymbol{u_{f,b}} \cdot \nabla \boldsymbol{d_s}) \cdot \boldsymbol{n}. \tag{2.21}$$

The dynamic boundary condition is obtained from the equality of the fluid and solid stresses at the common interface. Because the fluid is inviscid, the fluid stress at boundaries corresponds only to the pressure:

$$\boldsymbol{\sigma_s} \cdot \boldsymbol{n} = \boldsymbol{\sigma_f} \cdot \boldsymbol{n} = p\boldsymbol{n}. \tag{2.22}$$

Using the relation developed earlier between the fluid pressure and velocity potential (2.14), we can introduce the fluid velocity potential into the dynamic boundary condition:

$$\boldsymbol{\sigma_s} \cdot \boldsymbol{n} = \rho_f [\frac{\partial \phi}{\partial t} + (\boldsymbol{u_{f,b}} \cdot \nabla)\phi]\boldsymbol{n}. \tag{2.23}$$

On the fluid domain, we must also apply an impermeability condition on the upper and lower wall boundaries Γ_w. By setting the fluid velocity perturbation term u_f to zero and expressing it with the fluid velocity potential, we get the condition:

$$\nabla\phi = 0 \text{ on } \Gamma_w. \tag{2.24}$$

For the inlet Γ_i and outlet Γ_o boundaries, we expect the perturbation fluid velocity to dissipate at infinity. As such, we also expect the velocity potential to be null far from the oscillating plate:

$$\phi = 0 \text{ on } \Gamma_i \text{ and } \Gamma_o. \tag{2.25}$$

The effect of the size of the fluid domain before and after will be verified later to ensure it is sufficient to satisfy this assumption.

2.1.5 Modal decomposition

The final step to obtain the governing equations of our method is to introduce the harmonic form of our variables. We assume the small perturbation part of the solid displacement and fluid velocity potential can be expressed as harmonic fluctuations with the form:

$$\boldsymbol{d_s}(\boldsymbol{X}, t) = \tilde{\boldsymbol{d}}_{\boldsymbol{s}}(\boldsymbol{X})e^{i\omega t}, \tag{2.26}$$

$$\phi(\boldsymbol{X}, t) = \tilde{\phi}(\boldsymbol{X})e^{i\omega t}, \tag{2.27}$$

where ω is the complex frequency with the real and imaginary parts respectively representing the frequency and the decay rate. Terms with tilde represents the waveform of the mode. The tilde symbol is dropped from now on for legibility.

By introducing the modal decomposition of the solid displacement (2.26) and fluid velocity potential (2.27) into the continuity equation (2.12), the elasticity equation (2.5) and the boundary conditions (2.21), (2.23), (2.24) and (2.25), we get the following system of partial differential equations to solve:

$$\begin{cases} \rho_s - \omega^2 \boldsymbol{d_s} - \nabla \cdot \boldsymbol{\sigma_s}(\boldsymbol{d_s}) = 0 \quad \text{on } \Omega_s & (a) \\ \Delta\phi = 0 \quad \text{on } \Omega_f & (b) \\ \nabla\phi \cdot \boldsymbol{n} = (i\omega \boldsymbol{d_s} + \boldsymbol{u_{f,b}} \cdot \nabla \boldsymbol{d_s}) \cdot \boldsymbol{n} \quad \text{on } \Gamma_1,\Gamma_2,\Gamma_3 & (c) \\ \boldsymbol{\sigma_s} \cdot \boldsymbol{n} = \rho_f (i\omega\phi + \boldsymbol{u_{f,b}} \cdot \nabla\phi)\boldsymbol{n} \quad \text{on } \Gamma_1,\Gamma_2,\Gamma_3 & (d) \\ \nabla\phi = 0 \quad \text{on } \Gamma_w. & (e) \\ \phi = 0 \quad \text{on } \Gamma_i \text{ and } \Gamma_o. & (f) \end{cases} \tag{2.28}$$

From this system, we search the eigenvalues ω and their associated eigenvectors. These eigenvalues correspond to coupled oscillations of the fluid and solid domains. We are interested in finding the limit of stability. Thus, we are searching for the eigenvalues with the highest growth rate and their corresponding eigenvectors. These generally correspond to the first few eigenvectors with the smallest frequency.

2.1.6 Weak formulation

In the last section, we defined the strong form of our problem with (2.28). The finite element method is used to solve this set of equations for our test case and for other arbitrary geometries. To that end, in this section, the weak form of these equations is developed.

In the solid domain, we are searching for a solid displacement vector field such that $\boldsymbol{d_s} : \Omega_s \to \mathbb{R}^\alpha$ where $\alpha = 2$ or 3. The function $\boldsymbol{d_s}$ is defined in the Sobolev space $\boldsymbol{d_s} \in \mathcal{U}_s$ with:

$$\mathcal{U}_s = \{\boldsymbol{d_s} : \Omega_s \to \mathbb{R}^\alpha | \boldsymbol{d_s} \in \mathcal{H}^1(\omega_s), \boldsymbol{d_s} = 0 \text{ on } \Gamma_s^D\},$$

where Γ_s^D is the domain boundaries where a Dirichlet condition is applied. In the test case, this represents one or both ends of the plate. We also need to introduce the test function $\boldsymbol{e_s} \in \mathcal{U}_s$. By multiplying the elasticity equation with this test function and integrating over the domain, we obtain the following integral formulation:

$$\int_{\Omega_s} \rho_s \omega^2 \boldsymbol{d_s} \cdot \boldsymbol{e_s} dV + \int_{\Omega_s} (\nabla \cdot \boldsymbol{\sigma}(\boldsymbol{d_s})) \cdot \boldsymbol{e_s} dV = 0. \tag{2.29}$$

This last equation does not yet allow us to introduce the necessary boundary conditions. To do so, we introduce the first Green identity and get:

$$-\omega^2 \int_{\Omega_s} \rho_s \boldsymbol{d_s} \cdot \boldsymbol{e_s} dV + \int_{\Omega_s} \boldsymbol{\sigma}(\boldsymbol{d_s}) : \nabla \boldsymbol{e_s} dV - \int_{\Gamma_s} (\boldsymbol{\sigma}(\boldsymbol{d_s}) \cdot \boldsymbol{n}) \cdot \boldsymbol{e_s} dS = 0.$$

The last term in this equation allows us to apply the dynamic boundary condition (2.28)(d) of the fluid-structure interface. Doing so yields the weak form equation for the solid domain:

$$-\omega^2 \int_{\Omega_s} \rho_s \boldsymbol{d_s} \cdot \boldsymbol{e_s} dV + \int_{\Omega_s} \boldsymbol{\sigma}(\boldsymbol{d_s}) : \nabla \boldsymbol{e_s} dV + i\omega \int_{\Gamma_{fs}} \rho_f \phi \boldsymbol{n} \cdot \boldsymbol{e_s} dS + \int_{\Gamma_{fs}} \rho_f (\boldsymbol{u_{f,b}} \cdot \nabla \phi) \boldsymbol{n} \cdot \boldsymbol{e_s} dS = 0, \tag{2.30}$$

where Γ_{fs} is the fluid-structure interface. In the fluid domain, we are searching a velocity potential field such that $\phi : \Omega_f \to \mathbb{R}$. Function ϕ is defined on $\mathcal{P}$ with:

$$\mathcal{P} = \{\phi : \Omega_f \to \mathbb{R} | \phi \in \mathcal{H}^1, \phi = 0 \text{ on } \Gamma_f^D\},$$

where Γ_f^D is the fluid domain boundaries where a Dirichlet condition is applied. By introducing the test function $\psi \in \mathcal{P}$, we can obtain the integral formulation of the continuity equation (2.28)(b) in the fluid domain:

$$\int_{\Omega_f} \Delta \phi \psi dV = 0.$$

Just as in the solid domain, using the first Green identity introduces the term necessary to apply the boundary conditions:

$$\int_{\Omega_f} (\nabla \phi \cdot \nabla \psi) dV - \int_{\Gamma_f} (\nabla \phi \cdot \boldsymbol{n}) \psi dS = 0. \tag{2.31}$$

The last term is used to apply the kinematic boundary condition (2.28)(c). Doing so yields the weak form equation for the fluid domain:

$$\int_{\Omega_f} (\nabla \phi \cdot \nabla \psi) dV - i\omega \int_{\Gamma_2} (\boldsymbol{d_s} \cdot \boldsymbol{n}) \psi dS - \int_{\Gamma_2} (\boldsymbol{u_{f,b}} \cdot \nabla \boldsymbol{d_s}) \cdot \boldsymbol{n} \psi dS. \tag{2.32}$$

2.1.7 Matrix formulation

Equations (3.28) and (2.32) make up the weak form of our fluid-structure interaction problem. Introducing the following bi-linear operators is necessary to express it in matrix form:

$$\begin{aligned}
\mathcal{M}_s(\boldsymbol{d_s}, \boldsymbol{e_s}) &= \rho_s \int_{\Omega_s} \boldsymbol{d_s} \cdot \boldsymbol{e_s} dV \\
\mathcal{K}_s(\boldsymbol{u_s}, \boldsymbol{v}) &= \int_{\Omega_s} \boldsymbol{\sigma}(\boldsymbol{u_s}) : \epsilon(\boldsymbol{v}) dV \\
\mathcal{C}_{sf}(\phi, \boldsymbol{v}) &= \rho_f \int_{\Gamma_{fs}} \phi \boldsymbol{n} \cdot \boldsymbol{v} dS \\
\mathcal{K}_{sf}(\phi, \boldsymbol{v}) &= \rho_f \int_{\Gamma_{fs}} (\boldsymbol{u_{f,b}} \cdot \nabla \phi) \boldsymbol{n} \cdot \boldsymbol{v} dS \\
\mathcal{K}_f(\phi, \psi) &= \rho_f \int_{\Omega_f} (\nabla \phi \cdot \nabla \psi) dV \\
\mathcal{C}_{fs}(\boldsymbol{u_s}, \psi) &= \rho_f \int_{\Gamma fs} \boldsymbol{u_s} \cdot \boldsymbol{n} \psi dS \\
\mathcal{K}_{fs}(\boldsymbol{u_s}, \psi) &= \rho_f \int_{\Gamma_{fs}} (\boldsymbol{u_{f,b}} \cdot \nabla \boldsymbol{d_s}) \cdot \boldsymbol{n} \psi dS.
\end{aligned} \tag{2.33}$$

Our weak formulation can then be written as:

$$\begin{cases}
-\omega^2 \mathcal{M}_s + \mathcal{K}_s + i\omega \mathcal{C}_{sf} + \mathcal{K}_{sf} = 0 \\
\mathcal{K}_f - i\omega \mathcal{C}_{fs} - \mathcal{K}_{fs} = 0
\end{cases} \tag{2.34}$$

The matrix formulation is obtained by using the matrices resulting from the spatial discretization of the bi-linear operators. For example, the first bi-linear operator can be expressed as:

$$\mathcal{M}_s = \boldsymbol{E_s} \mathbb{M}_s \boldsymbol{D_s},$$

where $\boldsymbol{E_s}$ and $\boldsymbol{D_s}$ are the discretized vector of $\boldsymbol{e_s}$ and $\boldsymbol{d_s}$ respectively.

All the fluid-structure operators $\mathcal{C}_{sf}$, $\mathcal{K}_{sf}$, $\mathcal{C}_{fs}$ and $\mathcal{K}_{fs}$ are only defined on the interface of Ω_s and Ω_f, Γ_{fs}. To make the given matrix system consistent, the discretization is the same for both fluid and solid domains at their common boundary. By replacing all operators in (2.34), the problem becomes:

$$\left(\omega^2 \begin{bmatrix} -\mathbb{M}_s & 0 \\ 0 & 0 \end{bmatrix} + \omega \begin{bmatrix} 0 & i\mathbb{C}_{sf} \\ -i\mathbb{C}_{sf}^T & 0 \end{bmatrix} + \begin{bmatrix} \mathbb{K}_s & \mathbb{K}_{sf} \\ -\mathbb{K}_{fs} & \mathbb{K}_f \end{bmatrix} \right) \begin{bmatrix} \boldsymbol{D_s} \\ \boldsymbol{\Phi} \end{bmatrix} = 0, \tag{2.35}$$

where $\boldsymbol{D_s}$ and $\boldsymbol{\Phi}$ are the vectors representing the nodal values of $\boldsymbol{d_s}$ and ϕ respectively. It is also important to note that because of the similarity of $\mathcal{C}_{sf}$ and $\mathcal{C}_{fs}$, $\mathbb{C}_{fs} = \mathbb{C}_{sf}^T$.

By taking n_f and n_s to be the number of nodes in the fluid and solid domains respectively, vector $\boldsymbol{\Phi}$ has length n_f and vector $\boldsymbol{D_s}$ has length $2n_s$ because it includes displacement values in both dimensions. For example, the solid displacement vector corresponds to:

$$\boldsymbol{D_s} = [d_{s\,1}^x, d_{s\,1}^y, d_{s\,2}^x, d_{s\,2}^y, ..., d_{s\,n_s}^x, d_{s\,n_s}^y]^T,$$

2.2 Implementation details

2.2.1 Reduction of order

The problem (2.35) is a second-order eigenvalue problem with large non-symmetrical matrices. Although algorithms exist to solve second-order eigenvalue problems, they do not allow solving for a subset of the solutions. Considering our matrices represent a finite element discretization, their size requires an eigenvalue method with a memory usage that scales linearly with the size of the problem. Such a method is the implicitly restarted Arnoldi method that is implemented in the commonly used package ARPACK.

This method works for linear eigenvalue problems; thus, the first step is to reduce the order of our problem. By considering each block matrices of (2.35) as $\mathbb{M}$, $\mathbb{C}$ and $\mathbb{K}$ respectively, we can rewrite our eigenvalue problem as:

$$[\omega^2\mathbb{M} + \omega\mathbb{C} + \mathbb{K}]\boldsymbol{Y} = \boldsymbol{0}, \quad \text{with} \quad \boldsymbol{Y} = \begin{bmatrix} \boldsymbol{D_s} \\ \boldsymbol{\Phi} \end{bmatrix}. \tag{2.36}$$

Then, we can write the reduced order form for our eigenvalue problem as:

$$\left(\omega \begin{bmatrix} \mathbb{M} & 0 \\ 0 & \mathbb{K} \end{bmatrix} + \begin{bmatrix} \mathbb{C} & \mathbb{K} \\ -\mathbb{K} & 0 \end{bmatrix}\right)\boldsymbol{Z} = \boldsymbol{0}, \quad \text{with} \quad \boldsymbol{Z} = \begin{bmatrix} \omega\boldsymbol{Y} \\ \boldsymbol{Y} \end{bmatrix}. \tag{2.37}$$

By reintroducing the original matrices, we get the final problem that is solved for our potential method:

$$\left(\omega \begin{bmatrix} -\mathbb{M}_s & 0 & 0 & 0 \\ 0 & 0 & 0 & 0 \\ 0 & 0 & \mathbb{K}_s & \mathbb{K}_{sf} \\ 0 & 0 & -\mathbb{K}_{fs} & \mathbb{K}_f \end{bmatrix} + \begin{bmatrix} 0 & i\mathbb{C}_{sf} & \mathbb{K}_s & \mathbb{K}_{sf} \\ -i\mathbb{C}_{sf}^T & 0 & -\mathbb{K}_{fs} & \mathbb{K}_f \\ \mathbb{K}_s & \mathbb{K}_{sf} & 0 & 0 \\ -\mathbb{K}_{fs} & \mathbb{K}_f & 0 & 0 \end{bmatrix}\right) \begin{bmatrix} \omega\boldsymbol{D_s} \\ \omega\boldsymbol{\Phi} \\ \boldsymbol{D_s} \\ \boldsymbol{\Phi} \end{bmatrix} = \boldsymbol{0}. \tag{2.38}$$

2.2.2 Software implementation

All the sub-matrices in (2.38) are obtained using FreeFEM++ using the definition of the operators in (2.33). FreeFEM++ [37] is an open source partial-differential equation solver based on finite elements. It allows the simulation of multi-physics systems in 2D and 3D. FreeFEM++ scripts are written in a C++ idiom and are based on the weak formulation of PDE problems. It supports meshes from multiple generators such as GMSH [38] and also includes a built-in mesher BAMG.

To assemble the matrices of (2.38) and solve the eigenvalue problem, we used Matlab. Although these operations could have been done directly in FreeFEM++, the ease of use and strong support of Matlab made it worthwhile to write the code necessary to transfer the matrices to it. Matlab's function to solve sparse eigenvalue problems is *eigs*; it is based on ARPACK.

The solid displacement variable is discretized with quadratic continuous elements where the degrees of freedom are defined at the vertices and in the middle of each edge. The difference between the use of linear or quadratic elements for the solid domain is studied later. The fluid velocity potential is discretized with piecewise linear continuous finite elements where the degrees of freedom are defined at the vertices.

2.2.3 Mesh details and convergence analysis

For the potential method, the mesh generator built into FreeFEM++, BAMG, is used. It generates unstructured mesh with triangular elements. The mesh is specified by setting the number of nodes on each line composing our geometry.

In this section, we first evaluate the proper representation of the solid domain by doing a convergence analysis on the mesh using the first few eigenvalues of the linear elasticity problem. The asymptotic values are also compared to analytic values. Next, for the fluid domain, the influence of the mesh size close to the plate and at the outer boundaries is determined using convergence of the eigenvalues of the coupled problem. Finally, the effects of the size of the fluid domain behind the plate are evaluated. All simulations for the convergence analysis are done using the same mass and height ratios: $\mu = 1$ and $c = 1$.

The first step to validate our model is to ensure the linear elasticity part of our problem is properly implemented. To do so, we compute the eigenvalue problem of the plate without the fluid. By setting the fluid density to zero, $\rho_f = 0$, our potential method becomes the simple linear elasticity problem. Thus, to test the solid component of our model, we solve

the following eigenvalue problem:

$$(-\omega^2 \mathbb{M}_s + \mathbb{K}_s)\boldsymbol{D_s} = 0, \tag{2.39}$$

where the matrices $\mathbb{M}_s$ and $\mathbb{K}_s$ are the result of the discretization of the same operators as defined in (2.33). For the convergence analysis, clamped-free boundary conditions were taken for the plate's extremities.

Considering the simplicity of the solid domain, a simple rectangle, the mesh is defined by the number of elements in the height of the plate, n_{hs}. The number of elements in the length of the plate, n_{Ls}, is set such that the elements' aspect ratio is close to one. If we define the ratio between the plate's thickness and length to be $r = h_p/L$, we can express the number of elements in the length of the plate as $n_{Ls} \approx n_{hs}/r$. As such, for the same number of elements in the thickness, a thicker plate has fewer elements in its length. To study the convergence of the solid mesh, we progressively increased n_{hs}. The mode frequencies of problem (2.39) were compared to those obtained using Euler-Bernoulli beam theory. The theoretical frequencies for a cantilever plates of infinite width can be expressed as:

$$\omega_{th} = \frac{\alpha^2}{L^2}\sqrt{\frac{D}{\rho_s h_p}}, \tag{2.40}$$

where α is a non-dimensional parameter computed a priori for different mode number and boundary conditions. In figure 2.2, we present the convergence of the first and second mode with the error of the simulated vibration frequency when compared with the theoretical one vibration, ω_s/ω_{th}. This error term is computed with:

$$er(\omega_s) = \frac{|\omega_s - \omega_{th}|}{\omega_{th}}. \tag{2.41}$$

In figure 2.2, we see that with linear elements, acceptable convergence, that we define here as an error at or below 1% could be attained with a very fine discretization. On the other hand, with quadratic elements, acceptable convergence is achieved with only one element in the height of the plate.

Although a coarse discretization is sufficient to evaluate the eigenvalues of the simple solid case, the coupled problem may require a finer discretization of the fluid-structure boundary. Ensuring that the solid and fluid meshes share common nodes at their interface greatly simplifies the implementation of our formulation. Thus, n_{hs} not only describes the discretization of the plate, but also the fineness of the fluid mesh near the plate.

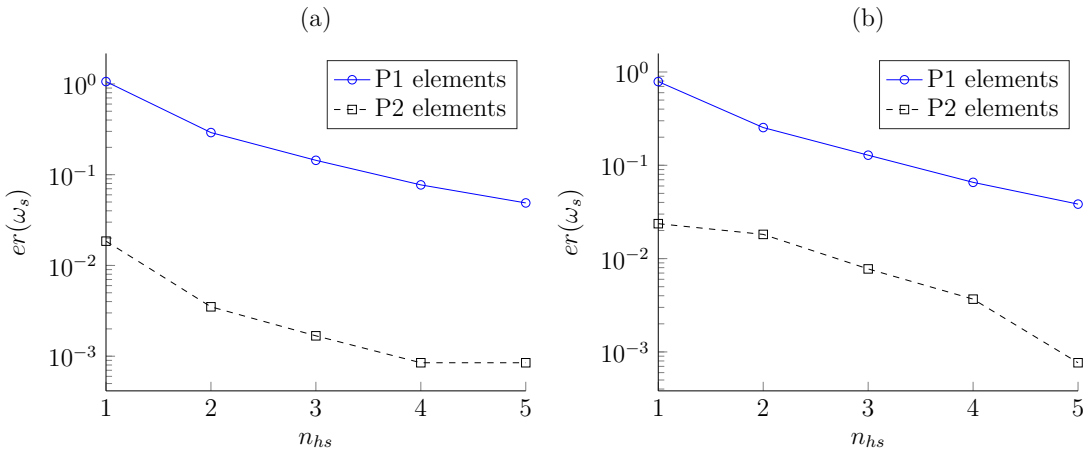

Figure 2.2 Convergence analysis of the solid domain discretization for the (a) first and (b) second modes. Error of the simulated vibration frequency for the first and second modes, when compared with the theoretical frequency, as a function of the number of elements in the height of the plate.

Overall, in our test case, there are three parameters that control the fluid mesh: the number of elements in the height of the plate n_{hs}, the plate height to length ratio r and the number of elements in the inlet and outlet of the fluid domain n_{hf}. Again, in the fluid domain, the number of elements on the horizontal boundaries is chosen to keep the aspect ratio of the elements close to unity.

To ensure that convergence has been achieved for the combined solid and fluid mesh, we keep n_{hs} fixed and vary r and n_{hf}. It was found above that $n_{hs} > 3$ is more than sufficient to obtain the eigenvalues of the solid problem if quadratic elements are used; this value is thus used from now on. Figure 2.3(a) shows the convergence of the frequencies of the plate in a fluid at rest with refinement of the fluid mesh close to the plate. The mesh resulting from a $r = 0.01$ is shown to be sufficient. Figure 2.3(b) shows that convergence of the mesh far from the plate is reached with few elements for the static fluid case. Both convergence analyses were done with cantilever boundary conditions and the error term, computed with (2.41), uses the values obtained with the finest mesh as reference frequencies.

With a fluid at rest, the fluid perturbation flow is simple and does not require a fine discretization far from the plate. With a mean flow, more attention is required to the fluid mesh. Thus, a convergence on the mesh far from the plate is shown in figure 2.4(a). These results were obtained by keeping the plate ratio $r = 0.01$. Just as in the static case, the discretization of the fluid domain in the wake of the plate seems to be sufficient with $n_{hf} = 8$.

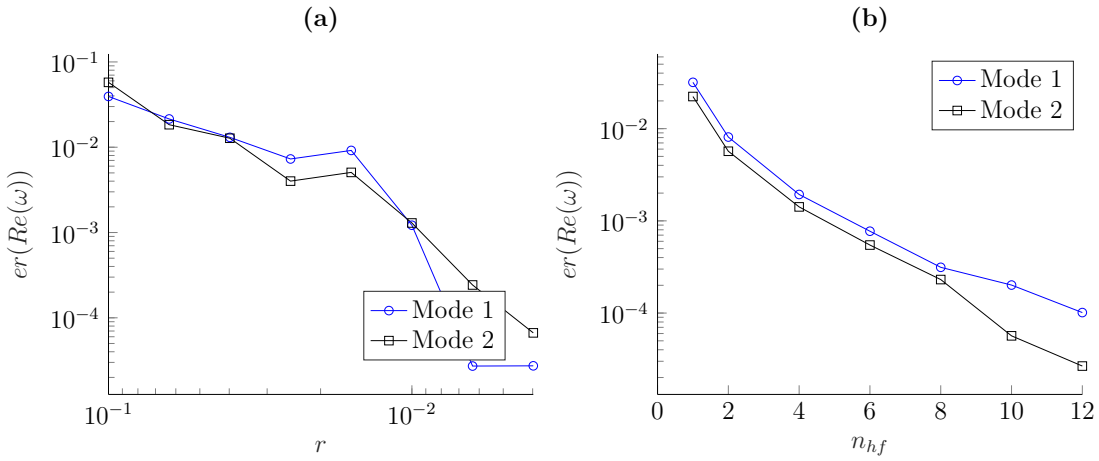

Figure 2.3 Convergence analysis of the fluid domain discretization for the coupled problem without base flow: impact of the height to length ratio r (a) and the number of elements in the height of the fluid domain boundaries n_{hf} (b) on the error of vibration frequencies for the first two coupled modes.

Proper representation of the wake is also dependant on the length of the fluid domain aft of the plate. Until now, the length of the fluid domain before the plate L_i and after the plate L_o were set at five times the length of the plate. Figure 2.4(b) shows the influence of $r_{Lo} = L_o/L$ on the convergence of the coupled modes frequencies. A value $r_{Lo} = 5$, as was used in the other convergence analyses, is shown to be sufficient.

From our convergence analysis, we obtain a proper discretization for the test case that is presented in figure 2.5. It uses the following parameters: $n_{hs} = 3$, $r = 0.01$, $n_{hf} = 8$ and $r_{Lo} = 5$.

2.3 Results

To study the behavior and applicability of the potential method, a parametric analysis on the reduced speed is done for two different sets of boundary conditions of the plate: cantilever and fixed-fixed. The results obtained with our simulations are compared with those of Guo and Paidoussis [1], referred here as $\bar{\omega}_{ref}$. For both boundary cases, the mass ratio and height ratio are set to $\mu = 1$ and $c = 1$.

For each eigenvalue obtained from the potential method, we also got its conjugate. The results presented here ignore the eigenvalues with a negative real part. The first modes are defined as those having the eigenvalues with the smallest positive real part.

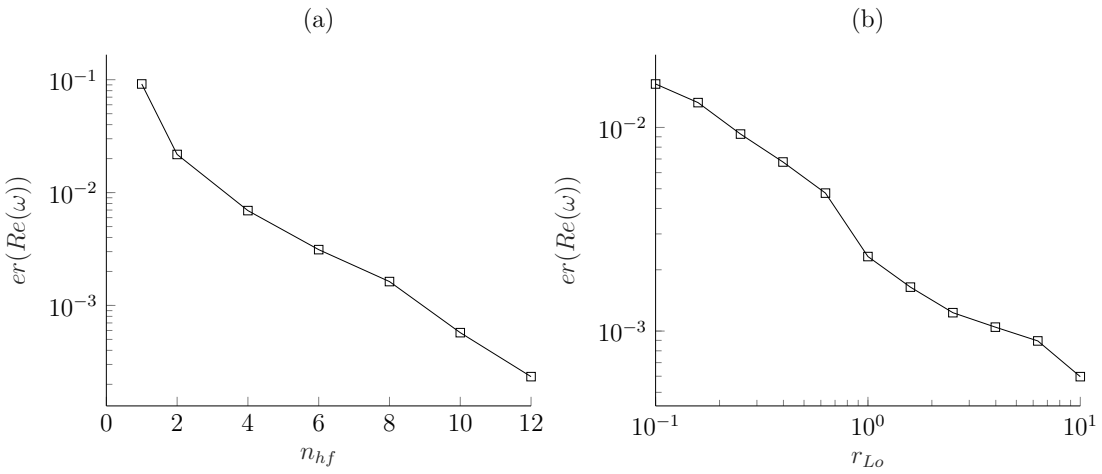

Figure 2.4 Convergence analysis of the fluid domain discretization for the coupled problem with a base flow of $U_R = 10$: impact on the error of the vibration frequency of the first coupled mode of (a) the number of elements in the height of the fluid domain n_{hf} and (b) the length of the fluid domain aft of the plate as ratio of the plate's length r_{Lo}.

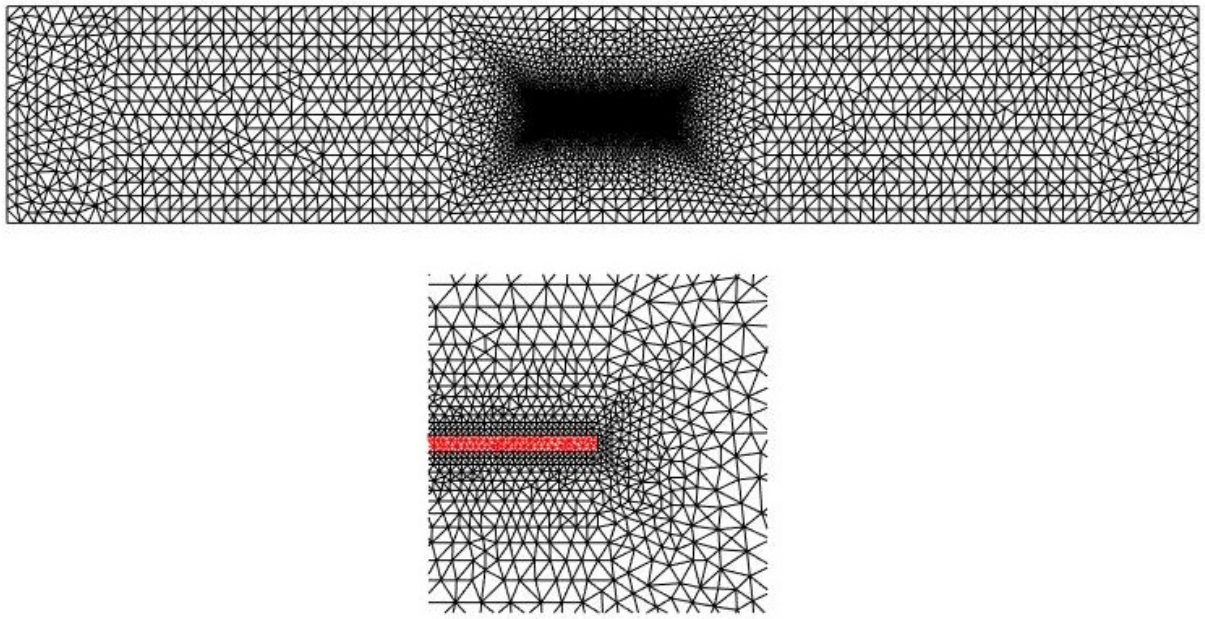

Figure 2.5 Mesh used for stability analysis of a plate in a potential axial flow, generated with $n_{hs} = 3$, $r = 0.01$, $n_{hf} = 8$ and $r_{Lo} = 5$ and a close-up of the trailing edge.

2.3.1 Fixed-fixed condition

Figure 2.6 shows the first two eigenvalues $\bar{\omega}_1, \bar{\omega}_2$ versus the reduced speed U_R. The solid and dotted lines respectively represent the real and imaginary parts of the eigenvalues obtained with our method and the results from Guo and Paidoussis are shown with dashed and dash-dot lines.

Figure 2.6 shows that the stability of plates with fixed-fixed boundaries is properly reproduced with the potential method. Instability occurs with the first mode for a reduced speed of about 8 for both our method and reference. The evolution of the imaginary part differs; with the potential method, mode 1 ($\cdots\cdots$) returns to stability at $U_R \approx 15$, whereas Guo and Paidoussis found no restabilisation of mode 1 in the considered reduced velocity range. For the second mode, the evolution of the real part is close to our reference at low reduced speed and starts to diverge near the instability point; the reduced speed at which the second mode becomes unstable is lower for the potential method than in the reference results.

Figure 2.7 shows the first and second eigenvectors with a fluid at rest and with a mean flow. It displays the perturbation velocity potential and the solid displacement of the plate. The eigenvectors obtained from solving problem 2.38 have complex components. Although the matrices of this system are real, complex eigenvectors arise because our damping matrix is non-proportional to the mass or stiffness matrix [39]. To properly represent each mode, we display the realization of the complex modes, which corresponds to the vector of the modulus of each component signed with their real part [40]. The mode shape displayed $\mathcal{V}$ is defined as:

$$\mathcal{V}_i = sgn(Re(\boldsymbol{Y}_i))|\boldsymbol{Y}_i|, \tag{2.42}$$

where sgn is the sign function. This equation yields the maximum envelope of each mode. The real or imaginary parts cannot be used independently to represent the mode shape as they also contain phase information.

Without flow, the modes, shown in figure 2.7(a) and (c), correspond to what is expected from an oscillating plate in a fluid. We see the perturbation velocity potential reaches maximums on the plate's boundary, where it is subject to the largest displacement. For the cases with a base flow, the relation between both domains is not as simple; the maximum perturbation velocity potential is not located at the maximum solid displacement. At speeds where the modes becomes unstable, an additional node in the fluid velocity potential appears on the fluid-structure boundary, near the leading edge of the plate.

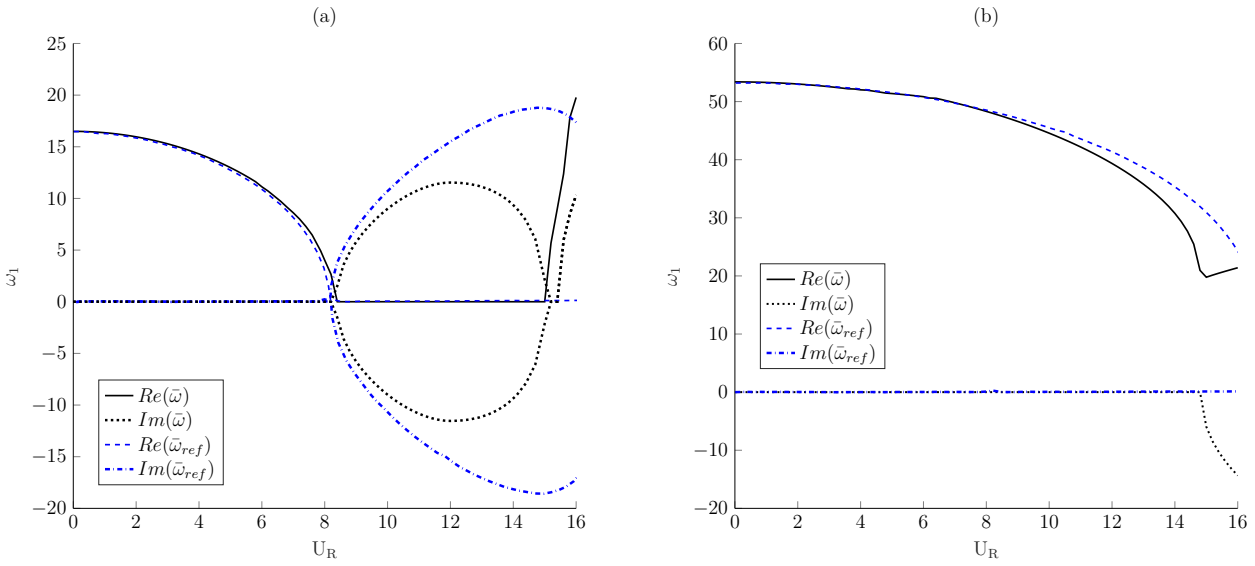

Figure 2.6 Stability analysis of a fixed-fixed plate: eigenvalues of the first (a) and second (b) modes as a function of the reduced speed. Solid and dotted lines are real and imaginary parts of the eigenvalues obtained from the potential method $\bar{\omega}$ and the dashed and dash-dotted lines are the real and imaginary parts of the eigenvalues from Guo and Paidoussis $\bar{\omega}_{ref}$ [1].

2.3.2 Cantilever condition

Figure 2.8 shows the stability analysis for the cantilever plate. As in the fixed-fixed case, the eigenvalues without a base flow obtained with our method are the same as in Guo and Paidoussis. On the other hand, the behavior of each mode with increasing reduced speed does not correspond to the reference results. The first mode becomes unstable at $U_R = 4$ unlike the reference were it remains stable for any speed. Just as the first mode, the behavior of the second mode is completely different. With the potential method, the second mode remains stable for all reduced speed; in the reference results, it predicts the instability of the plate at $U_R = 6$.

Similarly to the fixed-fixed plate, the mode shape, shown in figure 2.9, is as expected with a fluid at rest and gets more complex with increased reduced speed, when the mode becomes unstable.

2.3.3 Discussion

Although our potential method is solving a very similar set of equations as Guo and Paidoussis [1], a few differences remain. First, we simulate a plate with a finite thickness in a full domain,

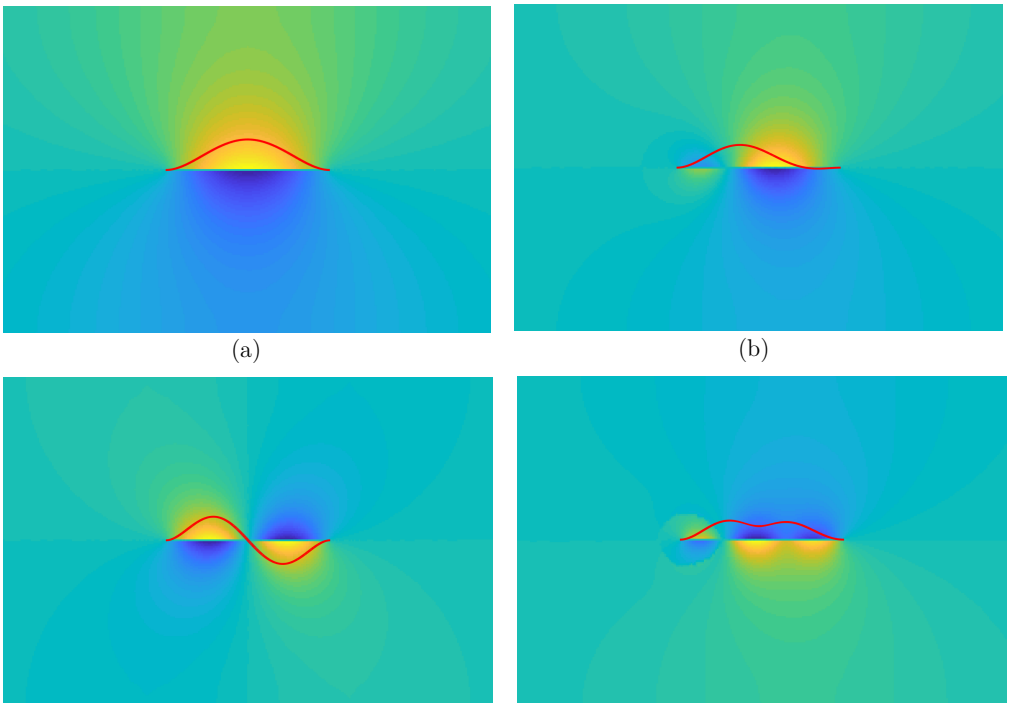

Figure 2.7 Mode shape representation for a plate with fixed-fixed boundary conditions. (a): 1st mode in a fluid at rest, (b): 1st mode with a reduced speed of $U_R = 10$ where the first mode is unstable, (c): 2nd mode in a fluid at rest, (d): 2nd mode with a reduced speed of $U_R = 15$ where the second mode is unstable.

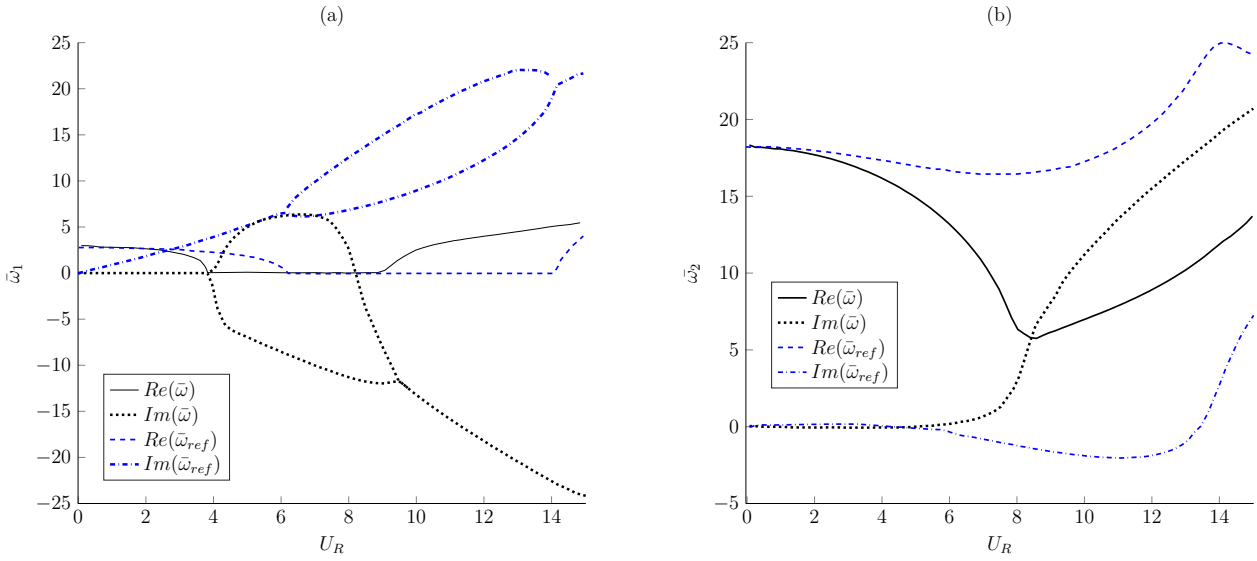

Figure 2.8 Stability analysis of a cantilever plate: eigenvalues of the first (a) and second (b) modes as a function of the reduced speed. Solid and dotted lines are real and imaginary parts of the eigenvalues obtained from the potential method and the dashed and dash-dotted lines are the real and imaginary parts of the eigenvalues from Guo and Paidoussis [1] $\bar{\omega}_{ref}$

.

Figure 2.9 Mode shape representation for a plate with fixed-fixed boundary conditions. (a): 1st mode in a fluid at rest, (b): 1st mode with a reduced speed of $U_R = 10$ where the first mode is unstable.

unlike the reference paper where the plate is infinitely thin and only half of the domain is considered. The second, and most significant difference, is the imposition of a wake condition in the perturbation velocity potential field. In Guo and Paidoussis, the wake is considered by imposing a null perturbation pressure in the wake of the plate. If we recall equation (2.14), this means imposing:

$$p = -\rho_f[i\omega\phi + (\boldsymbol{u_{f,b}} \cdot \nabla)\phi] = 0 \quad \text{on } \Gamma_{wake}. \tag{2.43}$$

Considering our simple geometry, the wake corresponds to $x > L, y = 0$. Thus, the wake condition can be simplified to:

$$\frac{\partial \phi}{\partial x} = \frac{i\omega\phi}{U} \quad \text{on } x > L, y = 0. \tag{2.44}$$

It seems like this condition could be imposed in the boundary term of the weak form of the continuity equation (2.31). But, when considering that the normal vector on the wake boundary is $\boldsymbol{n} = [0, 1]$, this term becomes:

$$\int_{\Gamma_f} (\nabla\phi \cdot \boldsymbol{n})\psi dS = \int_{\Gamma_{wake}} \frac{\partial \phi}{\partial y}\psi dS.$$

The derivative of the perturbation potential ϕ with respect to x naturally disappears from the wake boundary term of our weak formulation. Thus, the wake boundary condition (2.44) cannot be introduced into our formulation this way; our formulation does not allow for the imposition of a null pressure condition on a boundary parallel to the base flow. There is no other obvious method by which the wake condition can be introduced into our formulation.

The wake boundary difference between our method and the reference paper explains the fact the results for the fixed-fixed plate match and those for the cantilever plate do not. For the fixed-fixed boundary conditions, the wake does not play a significant role in the vibration behavior of the plate. The applicability of the potential method is thus limited to cases where the trailing edge of the solid is fixed. For other cases, even if the wake boundary condition was imposed, it would require a priori knowledge of the wake geometry. These major limitations prohibit the potential method to be used for most problems of interest. To solve this issue, introducing viscosity into the fluid equations allows the implicit consideration of the wake. This requires using the Navier-Stokes equations and is the subject of the next chapter.

CHAPTER 3 Navier-Stokes method

In this chapter, a method is developed to study the stability of an elastic solid in an incompressible viscous fluid flow. The addition of viscosity is the only fundamental difference with the potential method presented in the previous chapter, but it yields a vastly different formulation. The method presented here, herein referred to as the Navier-Stokes method, is similar to the potential method in that it also uses the small perturbation hypothesis and assumes harmonic forms of the perturbation variables. Here, the discretized eigenvalue problem is derived from the Navier-Stokes and linear elasticity equations, the implementation is detailed, and the results are compared with those from other equivalent methods.

The method described in this chapter is similar to the one presented by Fernandez and Le Tallec [35]. The manner in which the equations are developed is different, but the resulting eigenvalue problem is similar; the main differences result from the different treatment of the solid domain. Fernandez and Le Tallec used a reduced order solid which leads to simplifications of the solid domain equation and the fluid-structure boundaries.

The results presented here are selected to allow the comparison with two papers. The first, by Cisonni and al. [3], uses a time-marching coupled fluid-structure simulation method. The second is a recent paper by Pfister et al. [2] that is also based on Fernandez and Le Tallec [35]; it presents a linear stability analysis method similar to ours.

In the potential method, the lack of viscosity in the model was found to be a limiting factor. Without viscosity, the wake is not implicitly included and must be imposed through some condition. The classical wake condition for a potential flow proved not to be applicable within our formulation of the problem. In light of this, it was decided to include viscosity because it allows us to overcome the wake condition issue. It also brings our model closer to the physical reality of the problems of interest. For the problem of oscillations of hydroelectric turbine runners, it was previously found that the addition of viscosity is necessary to properly evaluate the natural frequencies and their associated damping factor [8]. Fundamentally, the addition of viscosity necessitates swapping the potential flow equation for the Navier-Stokes equations in the fluid domain.

3.1 Method details

The Navier-Stokes method aims to simulate the oscillations of a linear elastic solid in a viscous and incompressible Newtonian fluid. Similarly to the potential method, the focus of

this method is to determine the onset of instability. As such, our method is based on the small displacement hypothesis. It allows the linearization of the solid and fluid equations around a base configuration. The base configuration describes the base flow and the corresponding solid deformation defined from the reference configuration. Here, terms defined in the reference configuration are written with a $\hat{hat}$ symbol. Terms without it are defined in the base configuration.

3.1.1 Governing equations

In the potential method, the equations were developed assuming the base flow did not have an important influence on the base configuration of the solid domain. Although this assumption will also be taken for the test case used here, the equations are developed without it. Thus, we differentiate the reference configuration $\hat{\Omega}_s$ and $\hat{\Omega}_f$ and the base configuration Ω_s and Ω_f.

Just as in the potential method, the Navier-Stokes method uses the linear elasticity equation for the solid part of the model. The base governing equations in the solid domain Ω_s are thus:

$$\rho_s \frac{\partial^2 \hat{\boldsymbol{d}}_{\boldsymbol{s}}}{\partial t^2} - \nabla \cdot \hat{\boldsymbol{P}}(\hat{\boldsymbol{d}}_{\boldsymbol{s}}) = 0, \tag{3.1}$$

where $\hat{d}_s$ is the solid displacement, ρ_s is the solid density and $\hat{\boldsymbol{P}}$ is the first Piola-Kirchhoff stress tensor. It is defined as:

$$\hat{\boldsymbol{P}}(\hat{\boldsymbol{d}}_{\boldsymbol{s}}) = \hat{\boldsymbol{F}}(\hat{\boldsymbol{d}}_{\boldsymbol{s}})\hat{\boldsymbol{S}}(\hat{\boldsymbol{d}}_{\boldsymbol{s}}) \quad \text{with} \quad \hat{\boldsymbol{S}} = \lambda tr(\hat{\boldsymbol{E}}(\hat{\boldsymbol{d}}_{\boldsymbol{s}}))\boldsymbol{I} + 2\mu\hat{\boldsymbol{E}}(\hat{\boldsymbol{d}}_{\boldsymbol{s}}), \tag{3.2}$$

where $\hat{\boldsymbol{S}}$ is the second Piola-Kirchhoff stress tensor, $\hat{\boldsymbol{F}}(\hat{\boldsymbol{d}}_{\boldsymbol{s}}) = \boldsymbol{I} + \nabla(\hat{\boldsymbol{d}}_{\boldsymbol{s}})$ is the deformation gradient and $\hat{\boldsymbol{E}}$ is Lagrangian strain tensor. It is defined as :

$$\hat{\boldsymbol{E}}(\hat{\boldsymbol{d}}_{\boldsymbol{s}}) = \frac{1}{2}\Big(\hat{\boldsymbol{F}}^T(\hat{\boldsymbol{d}}_{\boldsymbol{s}})\hat{\boldsymbol{F}}(\hat{\boldsymbol{d}}_{\boldsymbol{s}}) - \boldsymbol{I}\Big). \tag{3.3}$$

By introducing the small perturbation hypothesis, we can decompose the total displacement $\hat{\boldsymbol{d}}_{\boldsymbol{s}}$ in the steady 0^{th} order displacement $\hat{\boldsymbol{d}}_{\boldsymbol{s,b}}$ caused by the base flow and the 1^{st} order perturbation term $\boldsymbol{d}_{\boldsymbol{s}}$:

$$\hat{\boldsymbol{d}}_{\boldsymbol{s}}(t) = \hat{\boldsymbol{d}}_{\boldsymbol{s,b}} + \boldsymbol{d}_{\boldsymbol{s}}(t). \tag{3.4}$$

All terms in equations (3.1) to (3.3) are defined in the reference configuration but we are interested in linearizing the solid equation around the base configuration. By using the decomposition (3.4), we can rewrite the Lagrangian strain tensor (3.3) by decomposing the

deformation gradient $\hat{\boldsymbol{F}}$ into a base and perturbation terms. We obtain :

$$\boldsymbol{E}(\boldsymbol{d_s}, \hat{\boldsymbol{d}}_{\boldsymbol{s,b}}) = \frac{1}{2}\Big(\hat{\boldsymbol{F}}^T(\hat{\boldsymbol{d}}_{\boldsymbol{s,b}})\boldsymbol{F}^T(\boldsymbol{d_s})\boldsymbol{F}(\boldsymbol{d_s})\hat{\boldsymbol{F}}(\hat{\boldsymbol{d}}_{\boldsymbol{s,b}}) - \boldsymbol{I}\Big). \tag{3.5}$$

Similarly to the standard Lagrangian strain tensor, the modified strain tensor (3.5) can be linearized and becomes:

$$\boldsymbol{E}(\boldsymbol{d_s}, \hat{\boldsymbol{d}}_{\boldsymbol{s,b}}) = \frac{1}{2}\Big(\hat{\boldsymbol{F}}^T(\hat{\boldsymbol{d}}_{\boldsymbol{s,b}})(\nabla \boldsymbol{d_s} + \nabla \boldsymbol{d}_{\boldsymbol{s}}^T)(\boldsymbol{d_s})\hat{\boldsymbol{F}}(\hat{\boldsymbol{d}}_{\boldsymbol{s,b}}) - \boldsymbol{I}\Big). \tag{3.6}$$

Applying the decomposition (3.4) to the first Piola-Kirchhoff stress tensor (3.2) thus gives:

$$\boldsymbol{P}(\boldsymbol{d_s}, \hat{\boldsymbol{d}}_{\boldsymbol{s,b}}) = \frac{1}{\hat{J}(\hat{\boldsymbol{d}}_{\boldsymbol{s,b}})}\boldsymbol{F}(\boldsymbol{d_s})\hat{\boldsymbol{F}}(\hat{\boldsymbol{d}}_{\boldsymbol{s,b}})\boldsymbol{S}(\boldsymbol{d_s}, \hat{\boldsymbol{d}}_{\boldsymbol{s,b}})\hat{\boldsymbol{F}}^T(\hat{\boldsymbol{d}}_{\boldsymbol{s,b}}), \tag{3.7}$$

where $\hat{J}$ is the determinant of the deformation gradient tensor in the reference configuration $\hat{\boldsymbol{F}}$ and $\boldsymbol{S}$ has the same definition here as in equation (3.2), except the Lagrangian strain tensor is replaced with the modified one defined in (3.6). By decomposing the deformation gradient $\boldsymbol{F}(\boldsymbol{d_s})$ and eliminating the second order terms, we get the linearized Piola-Kirchhoff stress tensor:

$$\boldsymbol{P'}(\boldsymbol{d_s}, \hat{\boldsymbol{d}}_{\boldsymbol{s,b}}) = \frac{1}{\hat{J}(\hat{\boldsymbol{d}}_{\boldsymbol{s,b}})}\Big(\nabla \boldsymbol{d_s}\hat{\boldsymbol{F}}(\hat{\boldsymbol{d}}_{\boldsymbol{s,b}})\hat{\boldsymbol{S}}(\hat{\boldsymbol{d}}_{\boldsymbol{s,b}})\hat{\boldsymbol{F}}^T(\hat{\boldsymbol{d}}_{\boldsymbol{s,b}}) + \hat{\boldsymbol{F}}(\hat{\boldsymbol{d}}_{\boldsymbol{s,b}})\boldsymbol{S}(\boldsymbol{d_s}\hat{\boldsymbol{d}}_{\boldsymbol{s,b}})\hat{\boldsymbol{F}}^T(\hat{\boldsymbol{d}}_{\boldsymbol{s,b}})\Big), . \tag{3.8}$$

With this linearized stress tensor, we can write the linearized form of the elasticity equation (3.1) around the base configuration:

$$\rho_s \frac{1}{\hat{J}(\hat{\boldsymbol{d}}_{\boldsymbol{s,b}})}\frac{\partial^2 \boldsymbol{d_s}}{\partial t^2} - \nabla \cdot \boldsymbol{P'}(\boldsymbol{d_s}, \hat{\boldsymbol{d}}_{\boldsymbol{s,b}}) = 0. \tag{3.9}$$

It is important to note that if the strain caused by the base flow are negligible, meaning that the reference and steady configuration are the same, the stress tensor (3.8) reduces to the Cauchy stress tensor.

While the solid displacement variable is defined with Lagrangian specification, the fluid variables are defined with an Eulerian one. Generally, trying to couple both frameworks would require the introduction of an ALE formulation, but the small perturbation hypothesis allows us to keep the Eulerian definition for the fluid equations. Unlike the solid domain where the differentiation between the reference and base configuration was essential to take into account the preloading of the structure, the fluid equations are expressed directly in the

base configuration. We start with the Navier-Stokes continuity and momentum equations:

$$\nabla \cdot \boldsymbol{U_f} = 0, \tag{3.10}$$

$$\rho_f \frac{\partial \boldsymbol{U_f}}{\partial t} + \rho_f (\boldsymbol{U_f} \cdot \nabla) \boldsymbol{U_f} - \nabla \cdot \boldsymbol{\sigma_f}(\boldsymbol{U_f}, P) = 0, \tag{3.11}$$

where $\boldsymbol{U_f}$ and P are the fluid velocity and pressure defined in the base configuration, ρ_f is the fluid density and $\boldsymbol{\sigma_f}(\boldsymbol{U_f})$ is the fluid Cauchy stress tensor. It is defined as:

$$\boldsymbol{\sigma_f}(\boldsymbol{U_f}, P) = -P\boldsymbol{I} + \boldsymbol{\tau_f}(\boldsymbol{U_f}), \tag{3.12}$$

where I is the identity matrix and $\boldsymbol{\tau_f}$ is the viscosity tensor. It is defined as:

$$\boldsymbol{\tau_f}(\boldsymbol{U_f}) = \mu_f(\nabla \boldsymbol{U_f} + \nabla \boldsymbol{U_f}^T),$$

where μ_f is the fluid viscosity. The term $\nabla \cdot \boldsymbol{\sigma_f}(\boldsymbol{U_f}, P)$ can thus be expressed as:

$$\nabla \cdot \boldsymbol{\sigma_f}(\boldsymbol{U_f}, P) = -\nabla P + \nabla \cdot \boldsymbol{\tau_f}(\boldsymbol{U_f}).$$

Similarly to the solid domain, we decompose the fluid variables into their base 0^{th} order and 1^{st} order small perturbation components:

$$\boldsymbol{U_f}(\boldsymbol{X}, t) = \boldsymbol{u_{f,b}}(\boldsymbol{X}) + \boldsymbol{u_f}(\boldsymbol{X}, t), \tag{3.13}$$

$$P(\boldsymbol{X}, t) = p_b(\boldsymbol{X}) + p(\boldsymbol{X}, t), \tag{3.14}$$

where $(\boldsymbol{u_{f,b}}, p_b)$ are the base flow velocity and pressure fields and $(\boldsymbol{u_f}, p)$ correspond to the perturbation flow fields. All these are defined on the base configuration domain Ω_f. By introducing this decomposition into the conservation and momentum equations, (3.10) and (3.11), they respectively become:

$$\nabla \cdot (\boldsymbol{u_{f,b}} + \boldsymbol{u_f}) = 0, \tag{3.15}$$

$$\rho_f \Big[\frac{\partial \boldsymbol{u_{f,b}} + \boldsymbol{u_f}}{\partial t} + ((\boldsymbol{u_{f,b}} + \boldsymbol{u_f}) \cdot \nabla)(\boldsymbol{u_{f,b}} + \boldsymbol{u_f}) \Big] + \nabla(p_b + p) - \nabla \cdot \boldsymbol{\tau_f}(\boldsymbol{u_{f,b}} + \boldsymbol{u_f}) = 0. \tag{3.16}$$

By developing each term in these equations, we get the 0^{th} order equations:

$$\nabla \cdot \boldsymbol{u_{f,b}} = 0, \tag{3.17}$$

$$\rho_f\Big[\frac{\partial \boldsymbol{u_{f,b}}}{\partial t} + (\boldsymbol{u_{f,b}} \cdot \nabla)\boldsymbol{u_{f,b}}\Big] + \nabla p_b - \nabla \cdot \boldsymbol{\tau_f}(\boldsymbol{u_{f,b}}) = 0, \tag{3.18}$$

and 1st order equations:

$$\nabla \cdot \boldsymbol{u_f} = 0, \tag{3.19}$$

$$\rho_f\Big[\frac{\partial \boldsymbol{u_f}}{\partial t} + (\boldsymbol{u_f} \cdot \nabla)\boldsymbol{u_{f,b}} + (\boldsymbol{u_{f,b}} \cdot \nabla)\boldsymbol{u_f} + (\boldsymbol{u_f} \cdot \nabla)\boldsymbol{u_f}\Big] + \nabla p - \nabla \cdot \boldsymbol{\tau_f}(\boldsymbol{u_f}) = 0. \tag{3.20}$$

The 0th order equations are solved in the base case computation and the results are used for solving the eigenvalue problem that results from the 1st order equations. The last convection term of equation (3.20), $(\boldsymbol{u_f} \cdot \nabla)\boldsymbol{u_f}$, can be neglected as it is the multiplication of two first-order terms.

Unlike the solid equation, the Navier-Stokes equations are expressed in an Eulerian framework. To make both formulations agree, particular attention must be given to the coupling boundary conditions. Just like in the potential method, we apply a dynamic and a kinematic boundary condition.

3.1.2 Fluid-structure boundary conditions

Kinematic boundary condition

For the kinematic boundary conditions, we start by equating the fluid and solid velocity at the common fluid-structure boundary Γ_{fs}:

$$\boldsymbol{U_f}(\boldsymbol{X} + \boldsymbol{d_s}, t) = \frac{\partial \boldsymbol{d_s}(\boldsymbol{X}, t)}{\partial t} \quad \text{on } \Gamma_{fs}. \tag{3.21}$$

The problem of coupling the kinematics of Eulerian fluid equations with a moving boundary was solved by Lighthill [31] with the transpiration velocity. This method allows the integration of the effects of a moving boundary in a fluid flow without the need to change the mesh. This method has been widely used for aeroelasticity problems in aeronautics.

The transpiration method considers the fluid-structure interface to be permeable. The fluid penetrates this boundary with a transpiration velocity that is defined as:

$$\boldsymbol{U_f}(\boldsymbol{X} + \boldsymbol{d_s}, t) = \boldsymbol{U_f}(\boldsymbol{X}, t) + \boldsymbol{d_s}(\boldsymbol{X}, t) \cdot \nabla \boldsymbol{U_f}(\boldsymbol{X}, t), \quad \text{on } \Gamma_{fs}.$$

The base fluid velocity field is assumed to be well defined and sufficiently regular in the vicinity of the fluid-structure interface. By combining this last equation with (3.21), we get

the following boundary condition:

$$\boldsymbol{U_f}(\boldsymbol{X},t) = \frac{\partial \boldsymbol{d_s}(\boldsymbol{X},t)}{\partial t} - \boldsymbol{d_s}(\boldsymbol{X},t)\cdot\nabla\boldsymbol{U_f}(\boldsymbol{X},t), \quad \text{on } \Gamma_{fs}.$$

Next, we apply the decomposition (3.13) in this boundary condition. It is important to note that in our base flow computation, the fluid-structure boundary uses a no-slip condition, meaning: $\boldsymbol{u_{f,b}}|_{\Gamma_{fs}} = 0$. From this, we get:

$$\boldsymbol{u_f} = \frac{\partial \boldsymbol{d_s}}{\partial t} - \boldsymbol{d_s}\cdot\nabla\boldsymbol{u_{f,b}} \quad \text{on } \Gamma_{fs}.$$

This last equation is obtained by neglecting the second order term $\boldsymbol{d_s}\cdot\nabla\boldsymbol{u_f}$ arising from the decomposition of $\boldsymbol{d_s}\cdot\nabla\boldsymbol{U_f} = \boldsymbol{d_s}\cdot\nabla\boldsymbol{u_{f,b}} + \boldsymbol{d_s}\cdot\nabla\boldsymbol{u_f}$. In the development of the weak formulation, the boundary condition that is actually applied includes the normal vector $\boldsymbol{n}$ of the boundary, that is defined as point outwards from the solid domain. The boundary condition thus becomes:

$$\boldsymbol{U_f}(\boldsymbol{X}+\boldsymbol{d_s},t)\cdot\boldsymbol{n} = \frac{\partial \boldsymbol{d_s}(\boldsymbol{X},t)}{\partial t}\cdot\boldsymbol{n} \quad \text{on } \Gamma_{fs}. \tag{3.22}$$

It is important to note that the normal of the boundary is affected by the displacement $\boldsymbol{d_s}$ of the structure. Thus, we must differentiate the time dependant normal $\boldsymbol{n}(\boldsymbol{X}+\boldsymbol{d_s},t)$ and the normal of the base configuration $\boldsymbol{n_b}(\boldsymbol{X})$. Using a similar development as above, it is then possible to rewrite (3.22) as:

$$\boldsymbol{u_f}\cdot\boldsymbol{n_b} = \frac{\partial \boldsymbol{d_s}}{\partial t}\cdot\boldsymbol{n} - (\boldsymbol{d_s}\cdot\nabla\boldsymbol{u_{f,b}})\cdot\boldsymbol{n} - \boldsymbol{u_f}(\boldsymbol{n}-\boldsymbol{n_b}) \quad \text{on } \Gamma_{fs}.$$

The difference in the base and deformed normal vectors is proportional to the deformation $\boldsymbol{d_s}$ causing it. Thus, considering our small perturbation hypothesis, this last term is a multiplication of two infinitesimal values and can be neglected. By neglecting other second order terms arising from the decomposition of the normal vector, the kinematic boundary condition becomes:

$$\boldsymbol{u_f}\cdot\boldsymbol{n_b} = \frac{\partial \boldsymbol{d_s}}{\partial t}\cdot\boldsymbol{n_b} - (\boldsymbol{d_s}\cdot\nabla\boldsymbol{u_{f,b}})\cdot\boldsymbol{n_b} \quad \text{on } \Gamma_{fs}. \tag{3.23}$$

Dynamic boundary condition

The dynamic boundary condition applied at the common fluid-structure boundary is obtained from equating the fluid and solid stress at the interface:

$$\boldsymbol{\sigma_f}(\boldsymbol{U_f}, P) = \boldsymbol{P}(\boldsymbol{d_s}, \hat{\boldsymbol{d}}_{\boldsymbol{s,b}}). \tag{3.24}$$

The linearization of the fluid stress tensor is developed in Fernandez and Le Tallec [35]. After introducing the decomposition (3.13) and accounting for the difference between the base and reference configuration, the dynamic boundary condition becomes:

$$\boldsymbol{\sigma_f}(\boldsymbol{u_f}, p) + \boldsymbol{d_s} \cdot \nabla \boldsymbol{\sigma_f}(\boldsymbol{u_{f,b}}, p_b) + \boldsymbol{\sigma_f}(\boldsymbol{u_{f,b}}, p_b) \cdot \boldsymbol{\eta}(\boldsymbol{d_s}) = \boldsymbol{P}(\boldsymbol{d_s}, \hat{\boldsymbol{d}}_{\boldsymbol{s,b}}) \quad \text{on } \Gamma_{fs}, \tag{3.25}$$

where $\boldsymbol{\eta}$ is a deformation operator defined as $\boldsymbol{\eta}(\boldsymbol{d_s}) = (\nabla \cdot \boldsymbol{d_s})\boldsymbol{I} - \nabla \boldsymbol{d_s}$. The first term $\boldsymbol{\sigma_f}(\boldsymbol{u_f}, p)$ corresponds to the perturbation fluid stress tensor. The second term $\nabla \boldsymbol{\sigma_f}(\boldsymbol{u_{f,b}}, p_b)\boldsymbol{d_s}$ corresponds to the impact of the solid displacement perturbation term on the base fluid stress and, when written with the Einstein notation, is:

$$[\boldsymbol{d_s} \cdot \nabla \boldsymbol{\sigma_f}(\boldsymbol{u_{f,b}}, p_b)]_{ij} = [\boldsymbol{d_s}]_k \frac{\partial [\boldsymbol{\sigma_f}(\boldsymbol{u_{f,b}}, p_b)]_{i,j}}{\partial x_k}.$$

The third term of equation $\boldsymbol{\sigma_f}(\boldsymbol{u_{f,b}}, p_b) \cdot \boldsymbol{\eta}(\boldsymbol{d_s})$, which is the product of two second order tensors, accounts for the impact of the variation of the normal vector on the base fluid stress [35].

3.1.3 Modal decomposition

After linearizing the fluid and solid equations, and the fluid-structure boundary conditions around a base configuration, we can write the partial derivative equations problem governing the Navier-Stokes method as:

$$\begin{cases} \rho_s \frac{1}{\hat{J}(\hat{\boldsymbol{d}}_{\boldsymbol{s,b}})} \frac{\partial^2 \hat{\boldsymbol{d}}_{\boldsymbol{s}}}{\partial t^2} - \nabla \cdot \boldsymbol{P}(\boldsymbol{d_s}, \hat{\boldsymbol{d}}_{\boldsymbol{s,b}}) = 0 \quad \text{on } \Omega_s & (a) \\ \nabla \cdot \boldsymbol{u_f} = 0 \quad \text{on } \Omega_f & (b) \\ \rho_f \Big[\frac{\partial \boldsymbol{u_f}}{\partial t} + (\boldsymbol{u_f} \cdot \nabla)\boldsymbol{u_{f,b}} + (\boldsymbol{u_{f,b}} \cdot \nabla)\boldsymbol{u_f} \Big] + \nabla p - \nabla \cdot \boldsymbol{\tau_f}(\boldsymbol{u_f}) = 0 \quad \text{on } \Omega_f & (c) \\ \boldsymbol{u_f} \cdot \boldsymbol{n_b} = \frac{\partial \boldsymbol{d_s}}{\partial t} \cdot \boldsymbol{n_b} - (\boldsymbol{d_s} \cdot \nabla \boldsymbol{u_{f,b}}) \cdot \boldsymbol{n_b} \quad \text{on } \Gamma_{fs} & (d) \\ \boldsymbol{\sigma_f}(\boldsymbol{u_f}, p) + \nabla \boldsymbol{\sigma_f}(\boldsymbol{u_{f,b}}, p_b)\boldsymbol{d_s} + \boldsymbol{\sigma_f}(\boldsymbol{u_{f,b}}, p_b) \cdot \boldsymbol{\eta}(\boldsymbol{d_s}) = \boldsymbol{P}(\boldsymbol{d_s}, \hat{\boldsymbol{d}}_{\boldsymbol{s,b}}) \quad \text{on } \Gamma_{fs} & (e) \end{cases} \tag{3.26}$$

Instead of solving this system of equations in the time domain, which would be computationally costly, we assume harmonic forms for the solid and fluid perturbation variables. This creates an eigenvalue problem that yields the vibration modes of the coupled system and their corresponding frequency and growth rate. The modal decomposition of the problem's variables is expressed as:

$$\begin{aligned}
\boldsymbol{d_s}(\boldsymbol{X}, t) &= \tilde{\boldsymbol{d}}_{\boldsymbol{s}}(\boldsymbol{X}) e^{i\omega t}, \\
\boldsymbol{u_f}(\boldsymbol{X}, t) &= \tilde{\boldsymbol{u}}_{\boldsymbol{f}}(\boldsymbol{X}) e^{i\omega t}, \\
p(\boldsymbol{X}, t) &= \tilde{p}(\boldsymbol{X}) e^{i\omega t},
\end{aligned}$$

where ω is the complex eigenvalue and $(\tilde{\boldsymbol{d}}_{\boldsymbol{s}}, \tilde{\boldsymbol{u}}_{\boldsymbol{f}}, \tilde{p})$ is the waveform of the modes. For legibility, the tilde symbol is dropped for the rest of the development. The eigenvalue problem that would result from (3.26) is quadratic because of the presence of the second order time derivative in the solid equation and the first time derivative in the fluid momentum equation. Solving a quadratic eigenvalue for the large matrices resulting from the spatial discretization of this problem would be problematic. Thus, following [41], a small perturbation solid displacement velocity is introduced:

$$\boldsymbol{u_s} = \frac{\partial \boldsymbol{d_s}}{\partial t}.$$

Applying this displacement velocity in the solid equation and applying the modal decomposition in (3.26), we get the linear eigenvalue problem:

$$\begin{cases}
i\omega \frac{\rho_s}{\hat{J}(\hat{\boldsymbol{d}}_{\boldsymbol{s},\boldsymbol{b}})} \boldsymbol{u_s} - \nabla \cdot \boldsymbol{P}(\boldsymbol{d_s}, \hat{\boldsymbol{d}}_{\boldsymbol{s},\boldsymbol{b}}) = 0 \quad \text{on } \Omega_s & (a) \\
i\omega \boldsymbol{d_s} = \boldsymbol{u_s} \quad \text{on } \Omega_s & (b) \\
\nabla \cdot \boldsymbol{u_f} = 0 \quad \text{on } \Omega_f & (c) \\
\rho_f \Big[i\omega \boldsymbol{u_f} + (\boldsymbol{u_f} \cdot \nabla) \boldsymbol{u}_{\boldsymbol{f},\boldsymbol{b}} + (\boldsymbol{u}_{\boldsymbol{f},\boldsymbol{b}} \cdot \nabla) \boldsymbol{u_f} \Big] + \nabla p - \nabla \cdot \boldsymbol{\tau_f}(\boldsymbol{u_f}) = 0 \quad \text{on } \Omega_f & (d) \\
\boldsymbol{u_f} \cdot \boldsymbol{n_b} = i\omega \boldsymbol{d_s} \cdot \boldsymbol{n_b} - (\boldsymbol{d_s} \cdot \nabla \boldsymbol{u}_{\boldsymbol{f},\boldsymbol{b}}) \cdot \boldsymbol{n_b} \quad \text{on } \Gamma_{fs} & (e) \\
\boldsymbol{\sigma_f}(\boldsymbol{u_f}, p) + \nabla \boldsymbol{\sigma_f}(\boldsymbol{u}_{\boldsymbol{f},\boldsymbol{b}}, p_b) \boldsymbol{d_s} + \boldsymbol{\sigma_f}(\boldsymbol{u}_{\boldsymbol{f},\boldsymbol{b}}, p_b) \cdot \boldsymbol{\eta}(\boldsymbol{d_s}) = \boldsymbol{P}(\boldsymbol{d_s}, \hat{\boldsymbol{d}}_{\boldsymbol{s},\boldsymbol{b}}) \quad \text{on } \Gamma_{fs} & (f)
\end{cases} \tag{3.27}$$

As we are interested in the limit of stability of this coupled system, we are searching for the eigenvectors with the highest growth rate. Although the order reduction of the eigenvalue problem could have been done using the same technique as in the potential method, introducing a displacement velocity yields smaller final matrices. Problem (3.27) is solved using a finite element formulation that is developed in the next section.

3.1.4 Weak formulation

To implement the method with finite elements, the weak form of problem (3.27) must first be defined. The solid displacement $\boldsymbol{d_s}$ and velocity $\boldsymbol{u_s}$ vector fields are defined on the same Sobolev space as in the potential method:

$$\boldsymbol{d_s}, \boldsymbol{u_s} \in \mathcal{U}_s = \{\boldsymbol{u} : \Omega_s \to \mathbb{R}^\alpha | \boldsymbol{u} \in \mathcal{H}^1(\Omega_s), \boldsymbol{u} = 0 \text{ on } \Gamma_s^D\}.$$

The fluid velocity and pressure fields are defined in similar Sobolev spaces as the solid variables:

$$\boldsymbol{u_f} \in \mathcal{U}_f = \{\boldsymbol{u} : \Omega_f \to \mathbb{R}^\alpha | \boldsymbol{u} \in \mathcal{H}^1(\Omega_f), \boldsymbol{u} = 0 \text{ on } \Gamma_f^D\},$$
$$p \in \mathcal{P}_f = \{\boldsymbol{p} : \Omega_f \to \mathbb{R} | p \in \mathcal{H}^1(\omega_f), p = 0 \text{ on } \Gamma_f^D\}.$$

In addition to the standard fluid fields, a Lagrangian multiplier is defined to write the weak formulation of the kinematic boundary condition. It is also used to weakly impose the dynamic boundary condition at the fluid-structure interface: $\lambda_f = \boldsymbol{\sigma_f}(\boldsymbol{u_f}, p) \cdot \boldsymbol{n}$. Thus, it is only defined on the interface:

$$\lambda \in \mathcal{L}_f = \{\lambda : \Gamma_{fs} \to \mathbb{R} | \lambda \in \mathcal{H}^1(\Gamma_f)\}.$$

To obtain the weak form of problem (3.27), we multiply the base solid and fluid equations by their associated test function and integrate over their domain. Development of the weak form solid equation is the same as in the potential method. Multiplying equation (3.27)(a) by a test function $\boldsymbol{e_s} \in \mathcal{U}_s$, integrating it over the solid domain and applying the first Green identity yields:

$$i\omega \int_{\Omega_s} \rho_s \boldsymbol{u_s} \cdot \boldsymbol{e_s} dV + \int_{\Omega_s} \boldsymbol{P}(\boldsymbol{d_s}, \hat{\boldsymbol{d}}_{\boldsymbol{s,b}}) : \nabla \boldsymbol{e_s} dV - \int_{\Gamma_s} (\boldsymbol{P}(\boldsymbol{d_s}) \cdot \boldsymbol{n}) \cdot \boldsymbol{e_s} dS = 0.$$

The last term of this equation is used to introduce the dynamic fluid-structure boundary condition (3.27)(f) in the weak formulation:

$$\begin{aligned} i\omega \int_{\Omega_s} \rho_s \boldsymbol{u_s} \cdot \boldsymbol{e_s} dV + \int_{\Omega_s} \boldsymbol{P}(\boldsymbol{d_s}, \hat{\boldsymbol{d}}_{\boldsymbol{s,b}}) : \nabla \boldsymbol{e_s} dV - \int_{\Gamma_s} (\boldsymbol{\sigma_f}(\boldsymbol{u_f}, p) \cdot \boldsymbol{n}) \cdot \boldsymbol{e_s} dS \\ - \int_{\Gamma_s} [\Big(\boldsymbol{d_s} \cdot \nabla \boldsymbol{\sigma_f}(\boldsymbol{u_{f,b}}, p_b) + \boldsymbol{\sigma_f}(\boldsymbol{u_{f,b}}, p_b) \cdot \boldsymbol{\eta}(\boldsymbol{d_s})\Big) \cdot \boldsymbol{n}] \cdot \boldsymbol{e_s} dS = 0. \end{aligned}$$

The variable $\boldsymbol{\lambda_f}$ is introduced into the weak solid equation by replacing the normal fluid stress $\boldsymbol{\sigma_f}(\boldsymbol{u_f}, p) \cdot \boldsymbol{n}$ in the first boundary integral term:

$$i\omega \int_{\Omega_s} \rho_s \boldsymbol{u_s} \cdot \boldsymbol{e_s} dV + \int_{\Omega_s} \boldsymbol{P}(\boldsymbol{d_s}, \hat{\boldsymbol{d}}_{\boldsymbol{s,b}}) : \nabla \boldsymbol{e_s} dV - \int_{\Gamma_s} \boldsymbol{\lambda_f} \cdot \boldsymbol{e_s} dS$$
$$- \int_{\Gamma_s} [\Big(\boldsymbol{d_s} \cdot \nabla \boldsymbol{\sigma_f}(\boldsymbol{u_{f,b}}, p_b) + \boldsymbol{\sigma_f}(\boldsymbol{u_{f,b}}, p_b) \cdot \boldsymbol{\eta}(\boldsymbol{d_s})\Big) \cdot \boldsymbol{n}] \cdot \boldsymbol{e_s} dS = 0. \quad (3.28)$$

The weak form of the equation (3.27)(b), used to reduce the order of the problem, is obtained by multiplying by the test function $\boldsymbol{v_s} \in \mathcal{U}_s$. After integrating over the solid domain, we obtain:

$$i\omega \int_{\Omega_s} \boldsymbol{d_s} \cdot \boldsymbol{v_s} dV - \int_{\Omega_s} \boldsymbol{u_s} \cdot \boldsymbol{v_s} dV = 0. \quad (3.29)$$

For the fluid equations, we define fluid velocity, pressure and boundary test functions: $\boldsymbol{v_f} \in \mathcal{U}_f$, $q \in \mathcal{P}_f$ and $\boldsymbol{\gamma_f} \in \mathcal{L}_f$. The pressure test function is used for the continuity equation (3.27)(c) and, after integrating over the fluid domain, we obtain:

$$\int_{\Omega_f} \nabla \cdot \boldsymbol{u_f} q dV = 0. \quad (3.30)$$

For the momentum equation (3.27)(d), we multiply it by the test function $\boldsymbol{v_f}$, integrate over the fluid domain and obtain:

$$i\omega\rho_f \int_{\Omega_f} \boldsymbol{u_f} \cdot \boldsymbol{v_f} + \rho_f \int_{\Omega_f} ((\boldsymbol{u_f} \cdot \nabla)\boldsymbol{u_{f,b}} + (\boldsymbol{u_{f,b}} \cdot \nabla)\boldsymbol{u_f}) \cdot \boldsymbol{v_f} dV + \int_{\Omega_f} \nabla p \cdot \boldsymbol{v_f} dV$$
$$- \int_{\Omega_f} (\nabla \cdot \boldsymbol{\tau_f}(\boldsymbol{u_f})) \cdot \boldsymbol{v_f} dV = 0.$$

By applying the divergence theorem and the vector identity $(\nabla \cdot \boldsymbol{A})\phi = \nabla \cdot (\boldsymbol{A}\phi) - \nabla\phi \cdot \boldsymbol{A}$, where $\boldsymbol{A}$ is a vector or a second order tensor and ϕ is a scalar or a vector, this last equation becomes:

$$i\omega\rho_f \int_{\Omega_f} \boldsymbol{u_f} \cdot \boldsymbol{v_f} + \rho_f \int_{\Omega_f} ((\boldsymbol{u_f} \cdot \nabla)\boldsymbol{u_{f,b}} + (\boldsymbol{u_{f,b}} \cdot \nabla)\boldsymbol{u_f}) \cdot \boldsymbol{v_f} dV - \int_{\Omega_f} p(\nabla \cdot \boldsymbol{v_f}) dV$$
$$+ \int_{\Omega_f} \boldsymbol{\tau_f}(\boldsymbol{u_f}) : \nabla \boldsymbol{v_f} dV + \int_{\Gamma_f} (p\boldsymbol{n} - \boldsymbol{\tau_f}\boldsymbol{n}) \cdot \boldsymbol{v_f} dS = 0.$$

Recalling the definition of the fluid stress tensor (3.12), the last term of this equation can be written as $\boldsymbol{\sigma_f}\boldsymbol{n} \cdot \boldsymbol{v_f}$. Thus, we can introduce the fluid-structure boundary Lagrangian

multiplier in the momentum equation:

$$i\omega\rho_f \int_{\Omega_f} \boldsymbol{u_f}\cdot\boldsymbol{v_f} + \rho_f \int_{\Omega_f} ((\boldsymbol{u_f}\cdot\nabla)\boldsymbol{u_{f,b}} + (\boldsymbol{u_{f,b}}\cdot\nabla)\boldsymbol{u_f})\cdot\boldsymbol{v_f}dV - \int_{\Omega_f} p(\nabla\cdot\boldsymbol{v_f})dV$$
$$+ \int_{\Omega_f} \boldsymbol{\tau_f}(\boldsymbol{u_f}) : \nabla\boldsymbol{v_f}dV + \int_{\Gamma_f} p\boldsymbol{n}\cdot\boldsymbol{v_f} - \int_{\Gamma_f} (\boldsymbol{\tau_f}(\boldsymbol{u_f})\cdot\boldsymbol{n})\cdot\boldsymbol{v_f}dS - \int_{\Gamma_{fs}} \boldsymbol{\lambda_f}\cdot\boldsymbol{v_f}dS = 0. \quad (3.31)$$

For the kinematic boundary equation (3.27)(e), we use the boundary test function $\boldsymbol{\gamma_f} \in \mathcal{L}$:

$$i\omega \int_{\Gamma_{fs}} \boldsymbol{d_s}\cdot\boldsymbol{\gamma_f} - \int_{\Gamma_{fs}} (\boldsymbol{d_s}\cdot\nabla\boldsymbol{u_{f,b}})\cdot\boldsymbol{\gamma_f}dS - \int_{\Gamma_{fs}} \boldsymbol{u_f}\cdot\boldsymbol{\gamma_f}dS = 0. \quad (3.32)$$

By combining both solid equations (3.28) and (3.29), and the fluid equations (3.30), (3.31) and (3.32), the weak form of system (3.27) equation is expressed as:

$$\begin{cases} i\omega \int_{\Omega_s} \rho_s \boldsymbol{u_s}\cdot\boldsymbol{e_s}dV + \int_{\Omega_s} \boldsymbol{P}(\boldsymbol{d_s}, \hat{\boldsymbol{d}}_{\boldsymbol{s,b}}) : \nabla\boldsymbol{e_s}dV - \int_{\Gamma_{fs}} \boldsymbol{\lambda_f}\cdot\boldsymbol{e_s}dS \\ \quad - \int_{\Gamma_{fs}} [\Big(\boldsymbol{d_s}\cdot\nabla\boldsymbol{\sigma_f}(\boldsymbol{u_{f,b}}, p_b) + \boldsymbol{\sigma_f}(\boldsymbol{u_{f,b}}, p_b)\cdot\boldsymbol{\eta}(\boldsymbol{d_s})\Big)\cdot\boldsymbol{n}]\cdot\boldsymbol{e_s}dS = 0 \\ i\omega \int_{\Omega_s} \boldsymbol{d_s}\cdot\boldsymbol{v_s}dV - \int_{\Omega_s} \boldsymbol{u_s}\cdot\boldsymbol{v_s}dV = 0 \\ i\omega\rho_f \int_{\Omega_f} \boldsymbol{u_f}\cdot\boldsymbol{v_f} + \rho_f \int_{\Omega_f} ((\boldsymbol{u_f}\cdot\nabla)\boldsymbol{u_{f,b}} + (\boldsymbol{u_{f,b}}\cdot\nabla)\boldsymbol{u_f})\cdot\boldsymbol{v_f}dV - \int_{\Omega_f} p(\nabla\cdot\boldsymbol{v_f})dV \\ + \int_{\Omega_f} \boldsymbol{\tau_f}(\boldsymbol{u_f}) : \nabla\boldsymbol{v_f}dV + \int_{\Gamma_f} p\boldsymbol{n}\cdot\boldsymbol{v_f}dS - \int_{\Gamma_f} (\boldsymbol{\tau_f}(\boldsymbol{u_f})\cdot\boldsymbol{n})\cdot\boldsymbol{v_f}dS - \int_{\Gamma_{fs}} \boldsymbol{\lambda_f}\cdot\boldsymbol{v_f}dS = 0 \\ \int_{\Omega_f} \nabla\cdot\boldsymbol{u_f}qdV = 0 \\ i\omega \int_{\Gamma_{fs}} \boldsymbol{d_s}\cdot\boldsymbol{\gamma_f} - \int_{\Gamma_{fs}} (\boldsymbol{d_s}\cdot\nabla\boldsymbol{u_{f,b}})\cdot\boldsymbol{\gamma_f}dS - \int_{\Gamma_{fs}} \boldsymbol{u_f}\cdot\boldsymbol{\gamma_f}dS = 0 \end{cases}$$

To simplify the formulation of the above system of equations, we express each integral term as a bi-linear operator:

$$\mathcal{B}_s(\boldsymbol{u_s}, \boldsymbol{e_s}) = \int_{\Omega_s} \rho_s \boldsymbol{u_s}\cdot\boldsymbol{e_s}dV$$
$$\mathcal{A}_s(\boldsymbol{d_s}, \boldsymbol{e_s}) = \int_{\Omega_s} \boldsymbol{P}(\boldsymbol{d_s}, \hat{\boldsymbol{d}}_{\boldsymbol{s,b}}) : \nabla\boldsymbol{e_s}dV$$
$$\mathcal{D}_{sf,1}(\boldsymbol{\lambda_f}, \boldsymbol{e_s}) = \int_{\Gamma_{fs}} \boldsymbol{\lambda_f}\cdot\boldsymbol{e_s}dS$$
$$\mathcal{D}_{sf,2}(\boldsymbol{d_s}, \boldsymbol{e_s}) = \int_{\Gamma_{fs}} [\Big(\boldsymbol{d_s}\cdot\nabla\boldsymbol{\sigma_f}(\boldsymbol{u_{f,b}}, p_b) + \boldsymbol{\sigma_f}(\boldsymbol{u_{f,b}}, p_b)\cdot\boldsymbol{\eta}(\boldsymbol{d_s})\Big)\cdot\boldsymbol{n}]\cdot\boldsymbol{e_s}dS$$
$$\mathcal{B}_{sr}(\boldsymbol{d_s}, \boldsymbol{v_s}) = \int_{\Omega_s} \boldsymbol{d_s}\cdot\boldsymbol{v_s}dV$$
$$\mathcal{A}_{sr}(\boldsymbol{u_s}, \boldsymbol{v_s}) = \int_{\Omega_s} \boldsymbol{u_s}\cdot\boldsymbol{v_s}dV$$
$$\mathcal{B}_{fm}(\boldsymbol{u_f}, \boldsymbol{v_f}) = \int_{\Omega_f} \rho_f \boldsymbol{u_f}\cdot\boldsymbol{v_f}dV$$

$$\mathcal{A}_{fm,1}(\boldsymbol{u_f}, \boldsymbol{v_f}) = \int_{\Omega_f} \rho_f((\boldsymbol{u_f} \cdot \nabla)\boldsymbol{u_{f,b}} + (\boldsymbol{u_{f,b}} \cdot \nabla)\boldsymbol{u_f}) \cdot \boldsymbol{v_f} dV$$

$$\mathcal{A}_{fm,2}(p, \boldsymbol{v_f}) = \int_{\Omega_f} p(\nabla \cdot \boldsymbol{v_f}) dV$$

$$\mathcal{V}_{fm}(\boldsymbol{u_f}, \boldsymbol{v_f}) = \int_{\Omega_f} \boldsymbol{\tau_f}(\boldsymbol{u_f}) : \nabla \boldsymbol{v_f} dV$$

$$\mathcal{T}_{f,1}(p, \boldsymbol{v_f}) = \int_{\Gamma_f} p\boldsymbol{n} \cdot \boldsymbol{v_f} dS$$

$$\mathcal{T}_{f,2}(\boldsymbol{u_f}, \boldsymbol{v_f}) = \int_{\Gamma_f} (\boldsymbol{\tau_f}(\boldsymbol{u_f}) \cdot \boldsymbol{n}) \cdot \boldsymbol{v_f} dS$$

$$\mathcal{T}_{fs}(\boldsymbol{\lambda_f}, \boldsymbol{v_f}) = \int_{\Gamma_{fs}} \boldsymbol{\lambda_f} \cdot \boldsymbol{v_f} dS$$

$$\mathcal{A}_{fc}(\boldsymbol{u_f}, q) = \int_{\Omega_f} \nabla \cdot \boldsymbol{u_f} q dV$$

$$\mathcal{K}_{fs,1}(\boldsymbol{d_s}, \boldsymbol{\gamma_f}) = \int_{\Gamma_{fs}} \boldsymbol{d_s} \cdot \boldsymbol{\gamma_f} dS$$

$$\mathcal{K}_{fs,2}(\boldsymbol{d_s}, \boldsymbol{\gamma_f}) = \int_{\Gamma_{fs}} (\boldsymbol{d_s} \cdot \nabla \boldsymbol{u_{f,b}}) \cdot \boldsymbol{\gamma_f} dS$$

$$\mathcal{K}_{fs,3}(\boldsymbol{u_f}, \boldsymbol{\gamma_f}) = \int_{\Gamma_{fs}} \boldsymbol{u_f} \cdot \boldsymbol{\gamma_f} dS$$

Our problem can then be written as:

$$\begin{cases} i\omega\mathcal{B}_s(\boldsymbol{u_s}, \boldsymbol{e_s}) + \mathcal{A}_s(\boldsymbol{d_s}, \boldsymbol{e_s}) - \mathcal{D}_{sf,1}(\boldsymbol{\lambda_f}, \boldsymbol{e_s}) - \mathcal{D}_{sf,2}(\boldsymbol{d_s}, \boldsymbol{e_s}) = 0 \\ i\omega\mathcal{B}_{sr}(\boldsymbol{d_s}, \boldsymbol{v_s}) - \mathcal{A}_{sr}(\boldsymbol{u_s}, \boldsymbol{v_s}) = 0 \\ i\omega\mathcal{B}_{fm}(\boldsymbol{u_f}, \boldsymbol{v_f}) + \mathcal{A}_{fm,1}(\boldsymbol{u_f}, \boldsymbol{v_f}) - \mathcal{A}_{fm,2}(p, \boldsymbol{v_f}) + \mathcal{V}_{fm}(\boldsymbol{u_f}, \boldsymbol{v_f}) \\ \quad + \mathcal{T}_{f,1}(p, \boldsymbol{v_f}) - \mathcal{T}_{f,2}(\boldsymbol{u_f}, \boldsymbol{v_f}) - \mathcal{T}_{fs}(\boldsymbol{\lambda_f}, \boldsymbol{v_f}) = 0 \\ \mathcal{A}_{fc}(\boldsymbol{u_f}, q) = 0 \\ i\omega\mathcal{K}_{fs,1}(\boldsymbol{d_s}, \boldsymbol{\gamma_f}) - \mathcal{K}_{fs,2}(\boldsymbol{d_s}, \boldsymbol{\gamma_f}) - \mathcal{K}_{fs,3}(\boldsymbol{u_f}, \boldsymbol{\gamma_f}) = 0. \end{cases} \tag{3.33}$$

3.1.5 Matrix formulation

To solve problem (3.33), we discretize the fluid and solid vector spaces $\boldsymbol{d_s}, \boldsymbol{u_s}, \boldsymbol{u_f}, p$ and $\boldsymbol{\lambda_f}$ over their respective domain. Both domains are discretized using a structured mesh. Details of the mesh for our test case are presented later.

To implement our weak formulation, it is useful to write our system of equations with a matrix formulation. Using the discretization of the different vector fields, the operators of (3.33) can be expressed as matrices. For example, the first operator can be written as:

$$\mathcal{B}_s(\boldsymbol{u_s}, \boldsymbol{e_s}) = \tilde{\boldsymbol{e}}_s^T \mathbb{B}_s \tilde{\boldsymbol{u}}_s,$$

where $\tilde{\boldsymbol{e}}_s$ and $\tilde{\boldsymbol{u}}_s$ correspond to the discretized equivalent of the continuous solid variables. By doing a similar discretization to every operator, we can write the matrix formulation of our problem:

$$
i\omega \begin{bmatrix} 0 & \mathbb{B}_s & 0 & 0 & 0 \\ \mathbb{B}_{sr} & 0 & 0 & 0 & 0 \\ 0 & 0 & \mathbb{B}_{fm} & 0 & 0 \\ 0 & 0 & 0 & 0 & 0 \\ \mathbb{K}_{fs,1} & 0 & 0 & 0 & 0 \end{bmatrix} \begin{pmatrix} \tilde{\boldsymbol{d}}_s \\ \tilde{\boldsymbol{u}}_s \\ \tilde{\boldsymbol{u}}_f \\ \tilde{p} \\ \tilde{\boldsymbol{\lambda}}_f \end{pmatrix}
$$

$$
+ \begin{bmatrix} \mathbb{A}_s - \mathbb{D}_{sf,2} & 0 & 0 & 0 & -\mathbb{D}_{sf,1} \\ 0 & -\mathbb{A}_{sr} & 0 & 0 & 0 \\ 0 & 0 & \mathbb{A}_{fm,1} + \mathbb{V}_{fm} - \mathbb{T}_{f,2} & \mathbb{A}_{fm,2} + \mathbb{T}_{f,1} & -\mathbb{T}_{fs} \\ 0 & 0 & \mathbb{A}_{fc} & 0 & 0 \\ -\mathbb{K}_{fs,2} & 0 & -\mathbb{K}_{fs,3} & 0 & 0 \end{bmatrix} \begin{pmatrix} \tilde{\boldsymbol{d}}_s \\ \tilde{\boldsymbol{u}}_s \\ \tilde{\boldsymbol{u}}_f \\ \tilde{p} \\ \tilde{\boldsymbol{\lambda}}_f \end{pmatrix} = 0. \quad (3.34)
$$

The variables vector combines both vectorial variables $\tilde{\boldsymbol{d}}_s, \tilde{\boldsymbol{u}}_s, \tilde{\boldsymbol{u}}_f, \tilde{\boldsymbol{\lambda}}_f$ and a scalar variable $\tilde{p}$. To make the dimensions agree, the vectorial variables are expressed as one-dimensional vectors, just as in the potential method.

3.2 Implementation details

Just as in the potential method, we solve the eigenvalue problem (3.34) using Freefem++ and Matlab. The discretized matrices are computed with Freefem++ from the weak formulation of the bi-linear operators. The given large sparse linear eigenvalue problem is assembled and solved using Matlab and its *eigs* function.

In the solid domain, both the displacement and velocity use quadratic continuous elements. In the fluid domain, the velocity also uses quadratic elements. The pressure uses piecewise linear elements. This combination is used mainly because the same combination of Taylor-Hood elements is used to solve the base flow of our problem. The boundary fluid stress is discretized with 1D linear elements.

3.2.1 Test case description

For the Navier-Stokes method, the objective is to reproduce results obtained from a time-marching algorithm by Cisonni et al. [3]. Thus, our test case is the same: a semi-infinite cantilever plate in a parallel viscous channel flow. The thin plate has a bending stiffness of

D and is clamped at the end of a rigid plate and positioned in the middle of the channel flow. A schematic of the problem's geometry and main dimensions is shown in figure 3.1. The fluid domain's total length is the combination of the inlet's length L_i, the plate's length L_p and length of the fluid domain aft of the plate L_o. The fluid domain height is defined by the vertical distance h between the plate and the boundaries of the channel flow. The plate thickness h_p is small enough for the longitudinal rigidity to be much greater than the flexural rigidity. Thus, we assume negligible plate extension caused by the base flow.

We are trying to reproduce the stability characteristics of this simple geometry for low Reynolds flows ($Re \leq 1000$). Although the intended uses of our method often imply high Reynolds situations, this test case constitutes a first step in verifying the usability and validity of our method. Higher Reynolds number would require the introduction of turbulence modeling into the base flow computation and in the small perturbation formulation.

This problem is governed by five non-dimensional numbers: the reduced velocity U_R, the mass ratio μ, the length ratio c, the Reynolds number Re and the plate thickness ratio r:

$$U_R = L_p\sqrt{\frac{\rho_s h_p}{D}}U, \quad \mu = \frac{\rho_f L_p}{\rho_s h_p}, \quad c = \frac{h}{L_p}, \quad Re = \frac{U\rho_f h}{\mu_f}, \quad r = \frac{h_p}{L}.$$

3.2.2 Base flow computation

The development of the Navier-Stokes method is based on the *a priori* knowledge of the base configuration of the fluid flow and solid displacement ($\boldsymbol{d_{s,b}}, \boldsymbol{u_{f,b}}, p_b$). For the general case, obtaining this base configuration would require solving a coupled static FSI problem. With our particular test of reproducing results from [3], the displacement of the plate is omitted in the base case simulation.

To obtain the base flow of our problem replicating, we use a Newton method to solve the non-linear Navier-Stokes equations for laminar flow (3.17) and (3.18). We impose standard inlet, outlet and solid boundary conditions for a viscous flow. At both inlets Γ_i, above and below the plate, we impose a Dirichlet condition with a quadratic velocity profile given by $u_{in}(y) = 6U\frac{y}{h}(1 - \frac{y}{h})$ where U is the average flow velocity. On the outlet Γ_o, we impose a stress-free outflow with a Neumann condition. On the top and bottom walls of the channel,

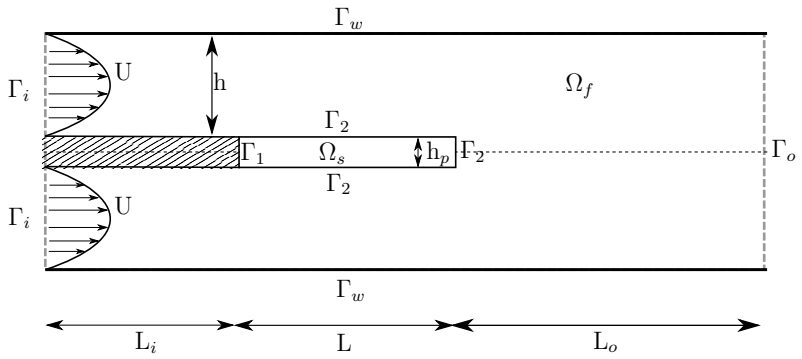

Figure 3.1 Schematic representation of the cantilever plate in a viscous parallel flow indicating the domains, boundaries and geometric measurements.

Γ_w, we impose a no-slip boundary. We are thus solving:

$$\begin{cases} \rho_f(\boldsymbol{u_{f,b}} \cdot \nabla)\boldsymbol{u_{f,b}} + \nabla p_b - \mu_f \Delta \boldsymbol{u_{f,b}} = 0 \quad \text{on } \Omega_f, \\ \nabla \cdot \boldsymbol{u_{f,b}} = 0 \quad \text{on } \Omega_f, \\ \boldsymbol{u_{f,b}} = [u_{in}, 0] \quad \text{on } \Gamma_i, \\ \boldsymbol{u_{f,b}} = \boldsymbol{0} \quad \text{on } \Gamma_w, \\ \mu \frac{\partial \boldsymbol{u_{f,b}}}{\partial \boldsymbol{n}} - p\boldsymbol{n} = \boldsymbol{0} \quad \text{on } \Gamma_o. \end{cases} \tag{3.35}$$

To solve this problem, we use the Newton method developed in the documentation of Freefem++ [37]. This method is exemplified with the backward facing step case and is based on work presented by Morgan et al. [42].

Results of the base flow computation for our test case at $Re = 50$ and $Re = 500$ are presented in figure 3.2. These results show the effect of an increase in viscosity. At low Reynolds, the fully developed flows above and below the plate combine rapidly and form a fully developed flow close to the trailing edge of the plate. At higher Reynolds, the flow requires a longer domain aft of the plate to regain a fully developed state. In both cases, the re-circulation zone behind the plate is minimal. The mesh used to solve the base flow is the same as the one used for the stability analysis.

3.2.3 Boundary conditions

Beyond the fluid-structure boundary, conditions for the rest of the domain must be set for the perturbation variables. On the upper and lower channel wall boundaries, we impose a

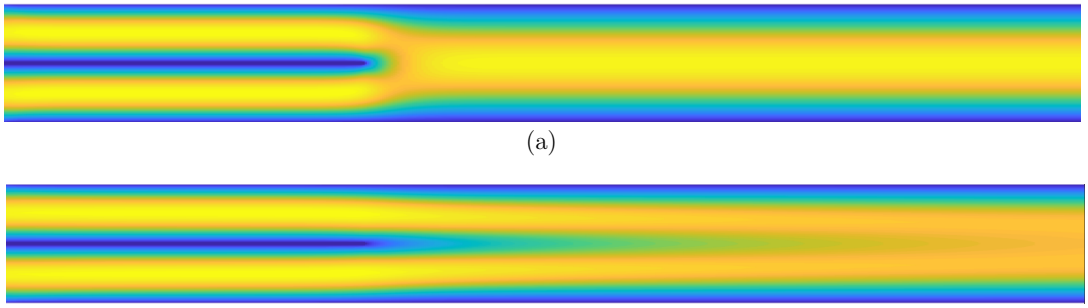

(a)

(b)

Figure 3.2 Results of the base flow computation for a semi-infinite cantilever plate in viscous flow with a Reynolds number of (a) 10 and (b) 500. The color gradient represents the axial flow velocity.

standard no-slip condition on the perturbation velocity field. On the inlet and outlet, stress-free boundary conditions are applied because it is assumed the perturbation velocity field will dissipate before reaching them. In our formulation, this corresponds to the natural boundary condition. Being a simple Dirichlet and natural Neumann boundary conditions, they can be imposed in our formulation and are expressed as:

$$\begin{aligned} \boldsymbol{u_f} &= \mathbf{0} \quad \text{on } \Gamma_w, \\ \boldsymbol{\sigma_f}(\boldsymbol{u_f}) &= 0 \quad \text{on } \Gamma_i \text{ and } \Gamma_o. \end{aligned}$$

3.2.4 Mesh details and convergence analysis

For the Navier-Stokes method, a structured mesh created with GMSH [38], an open-source finite element mesh generator, is used for the fluid and solid domains. A structured mesh is necessary to precisely control the mesh density around the plate and in its wake. Meshing parameters are selected to ensure that the elements' aspect ratio is close to unity near the plate. For the convergence analyses of the solid and a fluid meshes, the problem is solved with the following non-dimensional parameters: $U_R = 10$, $\mu = 2$, $c = 0.5$, $Re = 100$ and $r = 0.01$.

To ensure that the mesh is sufficiently dense, the eigenvalues obtained from multiple meshes, where the number of elements is approximately double between each, are compared. Tests for the solid domain's mesh are done without the influence of the fluid, by setting its density to zero. The results are compared to the theoretical frequencies obtained from the Euler-

Bernoulli beam theory (2.40), and the errors, computed with (2.41), are presented in figure 3.3.

Just as in the potential method, a coarse mesh is sufficient to properly estimate the solid vibration frequency. As the fluid and solid meshes share nodes at their interface, a finer solid discretization is necessary because it also impacts the fineness of the fluid mesh near the plate.

For the coupled domain, the results of the convergence analysis are presented in figure 3.4. The growth rate and frequency of the first mode reach an acceptable convergence, defined as an error at or below 1%, for a mesh with about 18000 elements. It was found through testing that the progressive element size variation allowed by a structured mesh is necessary to ensure that the sparse eigenvalue solver converges. Coarser and unstructured meshes may yield badly conditioned matrices in (3.34), such that the Arnoldi method, implemented in Matlab's eigenvalue solver *eigs*, may be unable to convergence to a solution.

For the stability analysis of the test case, the third mesh, comprised of 18244 triangular elements, is used. It is represented in figure 3.5. It can be seen that mesh density is increased near the plate's trailing edge, close to the upper and lower boundaries and in the direct wake of the plate.

3.2.5 Mode identification method

The identification of the coupled modes from the eigenvectors obtained from (3.34) is not trivial. Contrarily to the potential method where every eigenvector corresponds to a combination of a solid vibration mode and its impact on the fluid, the Navier-Stokes method yields multiple parasitic modes. These correspond to hydrodynamic modes where the fluid components of the mode are not related to structural motion. Examples of coupled and primarily hydrodynamic modes are presented in figure 3.6.

Figure (3.7) identifies the coupled and hydrodynamic modes in an Argand diagram of the eigenvalues of problem (3.34) for unstable conditions. Although the coupled modes are clearly separate from the hydrodynamic modes in this diagram, it may not always be the case with other parameter values. Defining an identification method more robust than visual inspection of the mode shapes is necessary to generalize the method. To that end, we define the solid and fluid strain energy in each mode as:

$$E_s = \int_{\Omega_s} \frac{1}{2}\boldsymbol{\epsilon}(\boldsymbol{d_S}) : \boldsymbol{\sigma_s}(\boldsymbol{d_s})dV, \quad \text{and} \quad E_f = \int_{\Omega_f} \frac{1}{2}\boldsymbol{\epsilon}(\boldsymbol{u_f}) : \boldsymbol{\sigma_s}(\boldsymbol{u_f}, p)dV.$$

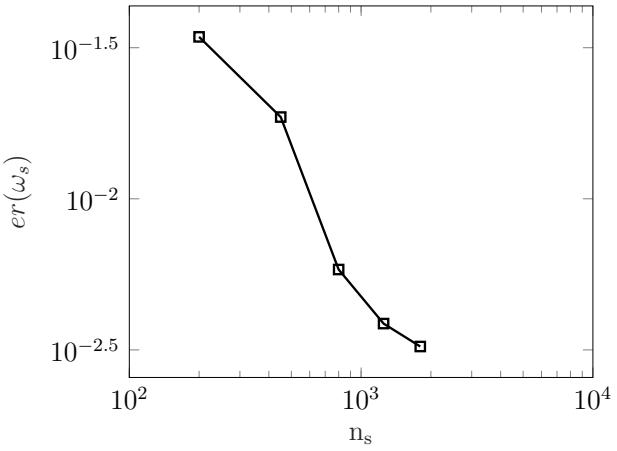

Figure 3.3 Convergence of the vibration frequency of the plate's first mode without fluid versus the number of elements in the solid mesh n_s. The order of convergence is 1.2. The error is obtained by comparing the simulated frequency with that of the Euler-Bernoulli beam theory. The simulations were made with $r = 0.01$.

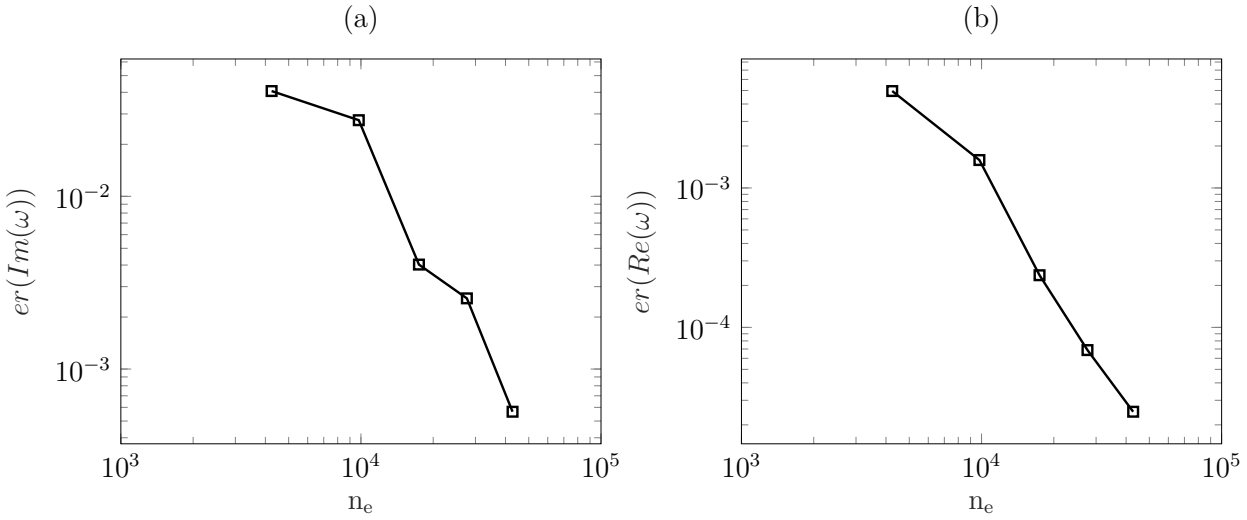

Figure 3.4 Convergence analysis of the (a) imaginary part and (b) real part of the first coupled mode eigenvalue versus the number of elements in the solid and fluid meshes n_e. The convergence rate of the imaginary and real parts are 1.8 and 2.4 respectively. Simulations made with $U_R = 10$, $\mu = 2$, $c = 0.5$, $Re = 100$ and $r = 0.01$. The error is computed by comparing the results with those obtained with the finest mesh.

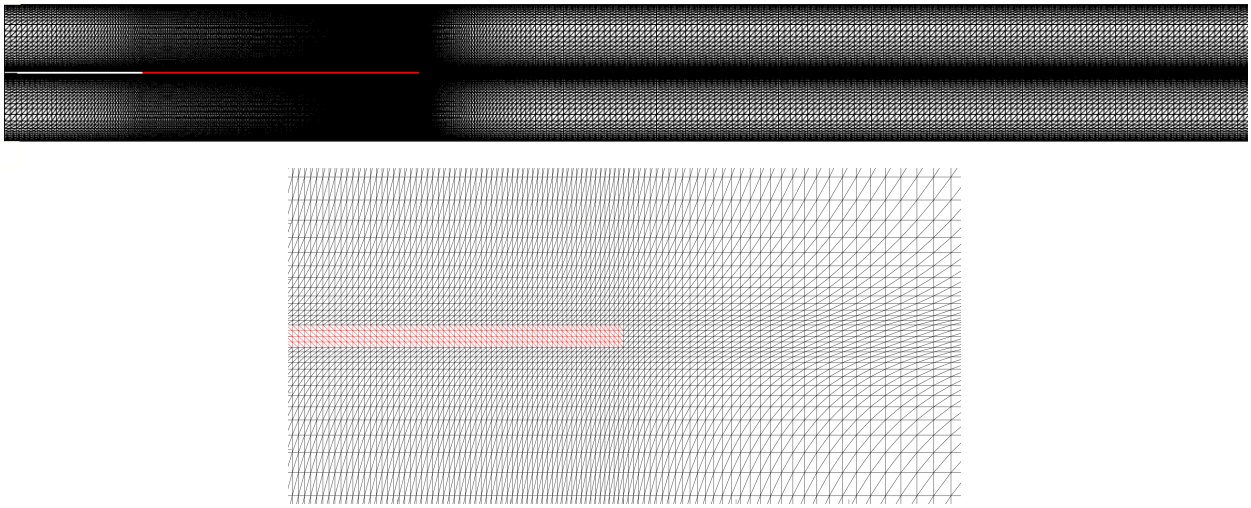

Figure 3.5 Mesh used for the stability analysis of the semi-infinite cantilever plate in an axial channel flow and a close-up of the plate's trailing edge.

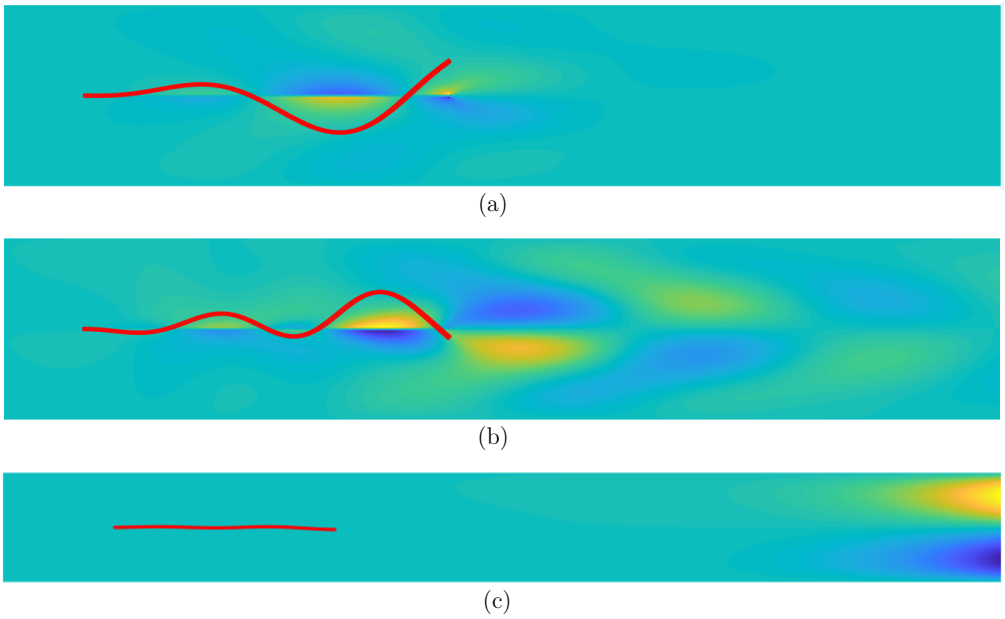

Figure 3.6 Mode shape representation for (a) the first and (b) second coupled modes and (c) a predominately hydrodynamic mode. All these modes result from problem (3.34) with $U_R = 30$, $\mu = 4$, $c = 0.5$, $Re = 100$ and $r = 0.01$.

The ratio of solid and fluid strain energy for each mode is presented in figure 3.8. The ratio for the coupled modes is at least three orders of magnitude greater than that of the hydrodynamic modes. This allows the easy identification of the modes of interest from all the eigenvectors computed with the Navier-Stokes method.

3.2.6 Mode tracking method

Computing a large number of eigenvectors and their energy ratio, to apply the mode identification method described above, is computationally heavy for large parametric analyses. Tracking a single or a few modes of interest is preferable. Here, we describe a continuation method used to track modes through the parametric analysis of the reduced speed U_R inspired by Hang et al. [43].

For the first value of U_R, a large quantity of solutions are computed from the eigenvalue problem (3.34). The modes of interest are identified with the energy ratio method. Their eigenvalues are then used as a reference for the next step of the parametric analysis; at the next U_R step, we ask the eigenvalue solver to only find the one solution with the closest eigenvalue. The eigenvector obtained is then compared to that of the mode identified at the previous reduced velocity. To ensure that it corresponds to the same mode, the modal assurance criterion (MAC) described by Pastor et al. [44] is used. The MAC number is defined as:

$$MAC(\boldsymbol{X_{i-1}}, \boldsymbol{X_i}) = \frac{|\boldsymbol{X_{i-1}} \cdot \boldsymbol{X_i}|^2}{(\boldsymbol{X_{i-1}} \cdot \boldsymbol{X_{i-1}})(\boldsymbol{X_i} \cdot \boldsymbol{X_i})},$$

where $\boldsymbol{X_i}$ and $\boldsymbol{X_{i-1}}$ represent the current and previous step eigenvectors. The MAC varies between 0 and 1 depending on how similar the modes are. We use a critical value of 0.9 to assess if the computed solution corresponds to the mode previously identified. If the MAC is below this threshold, the reduced velocity step is halved. This halving procedure is repeated until the critical MAC of 0.9 is reached. This ensures that, for any prescribed reduced velocity steps, the identified mode is correctly tracked.

It is important to note that to vary the reduced velocity, only the plate's Young's modulus is changed. Thus, between each iteration, only the sub-matrix related to this value, $\mathbb{A}_s$, needs to be recomputed. This greatly reduces the computation time required during such a parametric analysis. Similar shortcuts can be taken when studying other parameters.

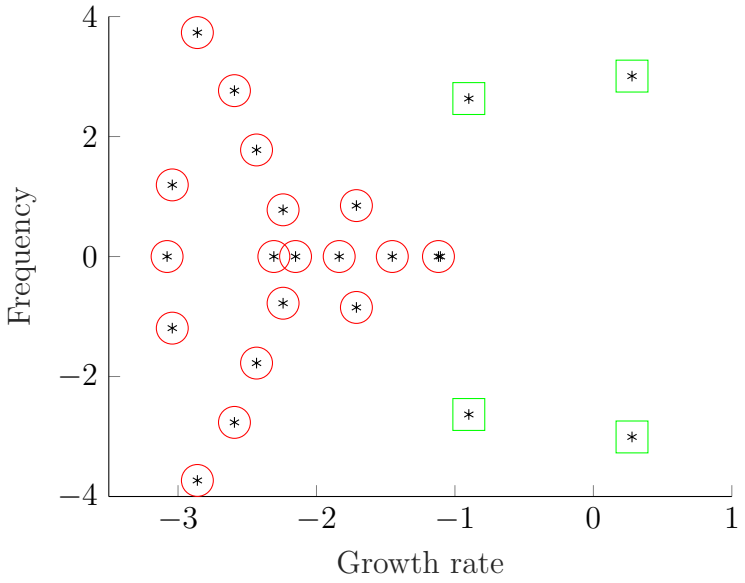

Figure 3.7 Argand diagram of the non-dimensional eigenvalues obtained for $U_R = 13.5$, $\mu = 4$, $c = 0.5$, $Re = 100$ and $r = 0.01$, where the frequency is $Re(\omega)$ and the growth rate is $-Im(\omega)$. Values inside green squares are associated with coupled modes and values circled in red are associated with hydrodynamic modes.

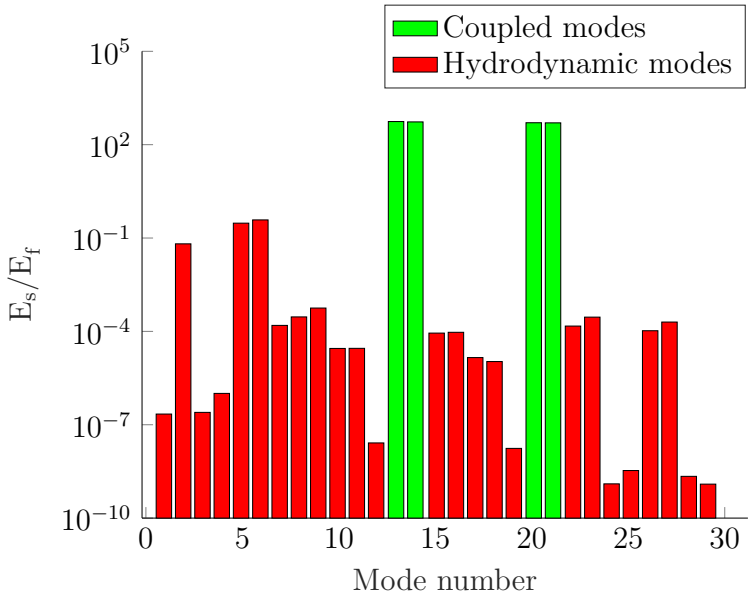

Figure 3.8 Energy ratio of the solid and fluid components of every mode given by the resolution of problem (3.34). Coupled modes have energy ratios at least three order of magnitude above any hydrodynamic mode.

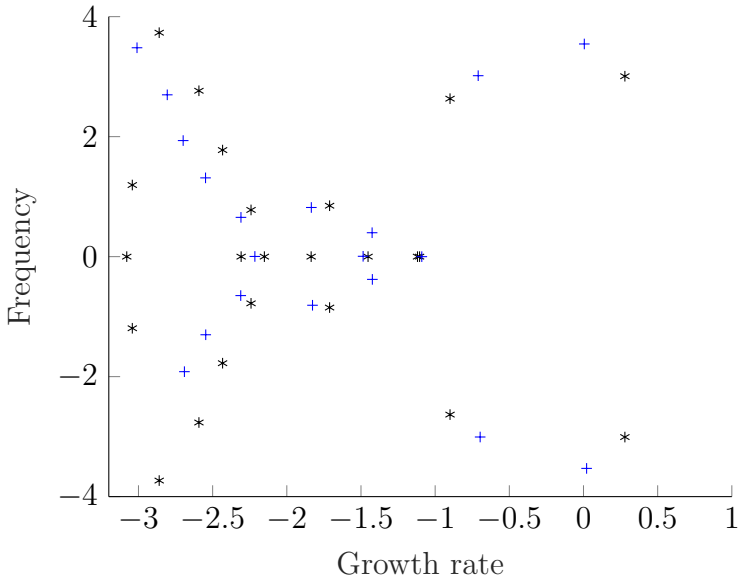

Figure 3.9 Comparison of the eigenvalues obtained with our method ($*$) and those from Pfister et al. [2] ($+$). Results are from non-dimensional parameters: $U_R = 13.53$, $\mu = 4$, $c = 0.5$, $Re = 100$ and $r = 0.01$.

3.3 Results

To verify the implementation of our method, we first reproduce the eigenvalues obtained by Pfister et al. [2] with $U_R = 13.53$, $\mu = 4$, $c = 0.5$, $Re = 100$ and $r = 0.01$. These results are presented in the Argand diagram of figure 3.9. Although both methods indicate that this set of conditions is unstable, the exact eigenvalues differ significantly. The method of Pfister et al. is also based on the coupling of linear elasticity and Navier-Stokes equations, but it uses a Lagrangian description of the fluid domain variables. This yields different coupling boundary conditions and the introduction of a third solid displacement extension variable. Beyond this difference, the base configuration computation used by Pfister et al. takes into account the impact of the fluid on the solid. Although the plate extension is minimal, and thus has no impact on the base flow, the tension in the plate does increase its rigidity and stability.

The impact of neglecting the tensioning of the plate by the base flow shear is also apparent in the evolution of eigenvalues with increasing reduced speed. Figure 3.10(a) and (b) presents the growth rate and frequency of the critical mode obtained with our method and compares it with equivalent results from Pfister et al. and Cisonni et al. The instability threshold predicted by both of these paper,$U_R = 13.3$ and $U_R = 13.5$ respectively, is higher than the one obtained with our method, $U_R = 11.9$. Including tensioning would naturally increase

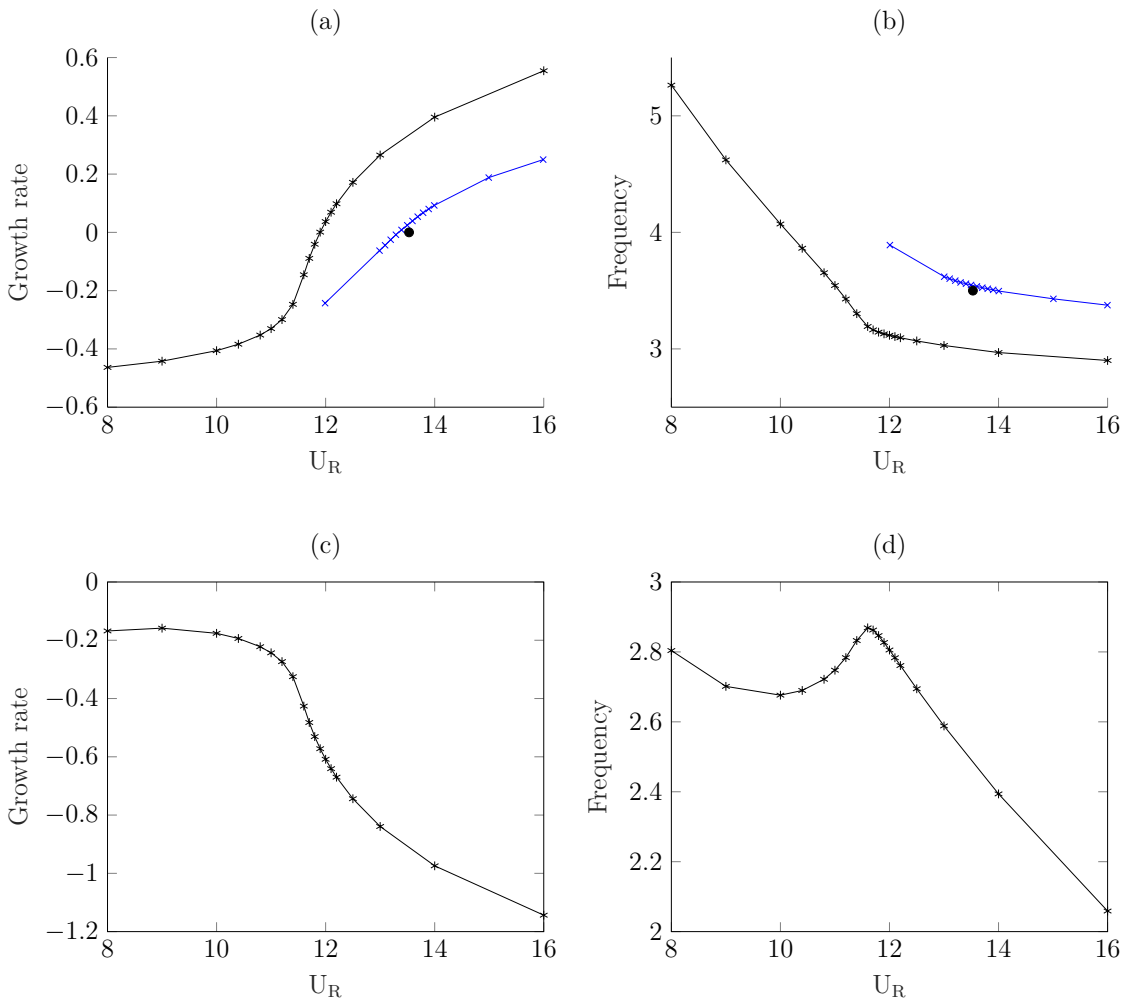

Figure 3.10 Evolution of the first two eigenvalues with increasing reduced speed U_R for $\mu = 4$, $c = 0.5$, $Re = 100$ and $r = 0.01$. (a) and (b) show the growth rate ($-Im(\omega)$) and the frequency ($Re(\omega)$) of the eigenvalue of the critical mode; it is depicted in figure 3.6(a). ($*$) corresponds to the results of our method, ($\times$) corresponds to results from Pfister et al. [2] and ($\bullet$) corresponds to results from Cisonni et al. [3]. (c) and (d) show the growth rate and frequency for the second coupled mode.

the frequencies we obtain and thus bring our results closer to those obtained by Cisonni and Pfister.

The results from Cisonni et al. [3] were obtained using a standard time-marching fluid-structure simulation method. They simulate the response of the plate to a small initial deformation. The growth rate is obtained by observing the decay or growth of the oscillations amplitude through time and the frequency is obtained with a Fourier analysis of the plate movement. The single point results of Cisonni presented in figure 3.10 took more than one CPU hour to obtain. On the other hand, a single point from our method can be obtained in less than one minute on a standard desktop computer. The computing limitation of our problem is not the computer power but the memory usage. The eigenvalue solver used in our implementation is not parallelized and its memory usage scales linearly with the number of degrees of freedom in the given problem. Two-dimensional test cases are solvable for standard computers but more complex three-dimensional problems may require specialized hardware equipped with large amounts of memory or an another eigenvalue solver.

Figure 3.10 also presents the evolution of the second coupled mode obtained from (3.34). These first two coupled modes correspond to those with the smallest eigenvalue modulus. It is interesting to note that the critical mode is not the one with the highest growth rate at low reduced speed. The second mode initially has a higher growth rate but it only decreases with increasing reduced speed. This illustrates the value of our mode tracking method because simply ordering the modes by growth rate wouldn't allow proper tracking through a parametric analysis. The critical mode described in figure 3.10(a) and (b) corresponds to the mode shape shown in figure 3.6(a) and the second mode of 3.10(c) and (d) corresponds to 3.6(b).

Impact of tensioning

Considering the base displacement of the plate due the base flow is neglected in the present implementation, tensioning of the plate is also omitted as it should normally be considered in the Piola-Kirchhoff stress tensor $\boldsymbol{P}(\boldsymbol{d_s}, \hat{\boldsymbol{d}}_{\boldsymbol{s,b}})$. In low Reynolds problems such as our test case, tensioning has a non-negligible impact; its omission leads the Navier-Stokes method to under-estimate the coupled system natural frequencies. To show that the tensioning has a non-negligible impact, a quick dimensional analysis is presented here. The tension T in our plate can be approximated to:

$$T = \int_0^L 2\tau_{xy} dx \quad \text{where} \quad \tau_{xy} = \mu_f \frac{\partial \boldsymbol{U_f}}{\partial y}.$$

By assuming the fluid flow profile remains constant across the length of the plate, i.e. $\boldsymbol{U_f} = [0, u_{in}]$, the base flow shear τ_{xy} and the tension can be written as:

$$\tau_{xy} = \mu_f \frac{\partial}{\partial y}[6U\frac{y}{h}(1-\frac{y}{h})] = \frac{6\mu_f U}{h} \quad \text{and} \quad T = 12\frac{\mu_f UL}{h}.$$

To compare the tension to the other non-dimensional parameters of our problem, a tension number defined as $\mathbb{T} = \frac{TL^2}{D}$ is introduced, where D is the bending stiffness of the plate. By using the reduced speed, Reynolds number and mass ratio, the tension number can be expressed as:

$$\mathbb{T} = 12\frac{U_R^2 \mu}{Re}.$$

By using the values of Re, U_R and μ that will be used later to compare the Navier-Stokes method to reference results ($Re = 100$, $U_R = 10$ and $\mu = 2$), we obtain a non-dimensional tension number of $\mathbb{T} = 24$. The relative scale of this value indicates that the tension in the plate is not negligible in the context of our test case. If the base configuration was computed using a coupled steady FSI solver, base displacement $\hat{\boldsymbol{d}}_{\boldsymbol{s,b}}$ could be used in the Piola-Kirchhoff stress tensor $\boldsymbol{P}(\boldsymbol{d_s}, \hat{\boldsymbol{d}}_{\boldsymbol{s,b}})$ to include tensioning in our model. This would result in better agreement with the reference results as it would increase the frequency of our eigenvalues.

CHAPTER 4 CONCLUSION

4.1 Summary of works

Two new approaches were proposed to evaluate the linear stability of structures immersed in a fluid flow. The first one, called here the potential method, is based on the combination of an inviscid and incompressible flow with a linear elastic solid to obtain an eigenvalue problem from which could be extracted the vibration modes of the coupled system and their respective frequency and growth rate. The corresponding equations were combined using an impermeability and stress transfer boundary conditions at the interface. After applying the small perturbation hypothesis and spatially discretizing using the finite element method, a second-order eigenvalue problem was obtained. The base flow is computed *a priori* with as potential flow. The method was compared to published results of the vibration of plates in a two-dimensional channel flow with various boundary conditions. The method was found to properly reproduce the stability properties of a fixed-fixed plate. For the cantilever boundary condition, it was found that the inability of our method to include a wake boundary condition was a limiting factor; the method does not correctly predict the onset of instability and which fundamental mode becomes unstable.

In order to avoid the wake boundary limitation, the addition of viscosity allows its implicit inclusion into the model. Thus, the second method was developed using the Navier-Stokes equation for the fluid. Just as in the potential method, careful consideration of the fluid-structure boundary, the small perturbation hypothesis and a finite element discretization allowed us to obtain an eigenvalue problem that could indicate the frequency and growth rate of the combined modes. Through this method, unwanted predominately hydrodynamic modes appear and need to be distinguished from the coupled modes of interest. To that end, mode identification and tracking methods were implemented and allowed us to conduct parameter analyses to compare our method with results obtained from a time-marching FSI method. The method was applied to a cantilever plate in a channel flow and compared to results from a standard FSI time-marching method, and to a method similar to ours. The instability threshold obtained with our method is slightly underestimated when compared with the reference results but offers a computational cost several orders of magnitude smaller.

4.2 Limitations and future research

The second method presented in this thesis, the Navier-Stokes method, remains limited to evaluating the ultimate threshold of instability; a modal analysis of the coupled fluid-structure system cannot evaluate the oscillation amplitude over time which is most important in the study of transient FSI phenomena in hydraulic turbines. Thus, our method is not a complete replacement of standard time-marching algorithms and should be seen as a preliminary step that could be used in the design phases for shape optimization algorithms. It could allow integrating a linear stability condition for such algorithms.

The difference between the results of the Navier-Stokes method presented here and the reference results is in part due to the omission of the tensionning of the plate by the base flow shear. This omission would not be as problematic for test cases with large Reynolds numbers but this would introduce additional challenges. As such, to apply this method to hydroelectric turbines, which are subject to high Reynolds flows, the complete computation of the static equilibrium base configuration would need to be implemented in addition to the consideration of turbulence in the fluid model. Also, further work on the well-posedness of our method needs to be done. On that note, the method published by Pfister et al. [2] is developed with the same objective as ours but their different formulation achieves better results. As such, understanding the fundamental differences between both approaches is another avenue to improve this type of method.

The numerical method used to solve the large and sparse eigenvalue problem obtained through our formulation, the Arnoldi method, is well established and is sufficiently efficient for our simple test cases. The limiting factor of this method is its memory usage. To compute the linear stability of a large and complex three-dimensional problem, specialized equipment or a new numerical method would be needed. Pre-conditioning of the current formulation or other mathematical manipulation may help alleviate this problem. Such advances would be necessary for the useful application of FSI coupled modal analysis methods such as the ones presented here.

REFERENCES

[1] C. Q. Guo and M. P. Paidoussis, "Stability of Rectangular Plates With Free Side-Edges in Two-Dimensional Inviscid Channel Flow," *Journal of Applied Mechanics*, vol. 67, no. 1, pp. 171–176, Mar. 2000.

[2] J.-L. Pfister, O. Marquet, and M. Carini, "Linear stability analysis of strongly coupled fluid–structure problems with the Arbitrary-Lagrangian–Eulerian method," *Computer Methods in Applied Mechanics and Engineering*, vol. 355, pp. 663–689, Oct. 2019.

[3] J. Cisonni, A. D. Lucey, N. S. Elliott, and M. Heil, "The stability of a flexible cantilever in viscous channel flow," *Journal of Sound and Vibration*, vol. 396, pp. 186–202, May 2017.

[4] E. d. Langre, *Fluides et solides*. Editions Ecole Polytechnique, 2001, google-Books-ID: IFnLwQ4eTIwC.

[5] E. H. Dowell and K. C. Hall, "Modeling of Fluid-Structure Interaction," *Annual Review of Fluid Mechanics*, vol. 33, no. 1, pp. 445–490, 2001.

[6] G. Hou, J. Wang, and A. Layton, "Numerical Methods for Fluid-Structure Interaction — A Review," *Communications in Computational Physics*, vol. 12, no. 2, pp. 337–377, Aug. 2012.

[7] A. S. Dehkharqani, J.-O. Aidanpää, F. Engström, and M. J. Cervantes, "A Review of Available Methods for the Assessment of Fluid Added Mass, Damping, and Stiffness With an Emphasis on Hydraulic Turbines," *Applied Mechanics Reviews*, vol. 70, no. 5, Sep. 2018.

[8] A. Coutu, C. Seeley, C. Monette, B. Nennemann, and H. Marmont, "Damping measurements in flowing water," *IOP Conference Series: Earth and Environmental Science*, vol. 15, no. 6, p. 062060, Nov. 2012.

[9] B. Hübner, U. Seidel, and S. Roth, "Application of fluid-structure coupling to predict the dynamic behavior of turbine components," *IOP Conference Series: Earth and Environmental Science*, vol. 12, p. 012009, Aug. 2010.

[10] T. Liaghat, F. Guibault, L. Allenbach, and B. Nennemann, "Two-Way Fluid-Structure Coupling in Vibration and Damping Analysis of an Oscillating Hydrofoil," in *Volume*

4A: Dynamics, Vibration, and Control. Montreal, Quebec, Canada: American Society of Mechanical Engineers, Nov. 2014, p. V04AT04A073.

[11] J. P. Gauthier, A. M. Giroux, S. Etienne, and F. P. Gosselin, "A numerical method for the determination of flow-induced damping in hydroelectric turbines," *Journal of Fluids and Structures*, vol. 69, pp. 341–354, Feb. 2017.

[12] T. Gjengedal, "Integration of wind power and the impact on power system operation," in *Large Engineering Systems Conference on Power Engineering, 2003.* Montreal, Que., Canada: IEEE, 2003, pp. 76–83.

[13] T. M. I. Mahlia, T. J. Saktisahdan, A. Jannifar, M. H. Hasan, and H. S. C. Matseelar, "A review of available methods and development on energy storage; technology update," *Renewable and Sustainable Energy Reviews*, vol. 33, pp. 532–545, May 2014.

[14] M. Sick, C. Oram, O. Braum, B. Nenneman, and A. Coutu, "Hydro projects delivering regulating power: Technical challenges and cost of operation," vol. 1, Innsbruck, Austria, Oct. 2013.

[15] T. Key, "Quantifying the Value of Hydropower in the Electric Grid: Final Report," Electric Power Research Institute, Technical report, Feb. 2013.

[16] X. Liu, Y. Luo, and Z. Wang, "A review on fatigue damage mechanism in hydro turbines - ScienceDirect," *Renewable and Sustainable Energy Reviews*, vol. 54, pp. 1–14, Feb. 2016.

[17] C. Trivedi, "A review on fluid structure interaction in hydraulic turbines: A focus on hydrodynamic damping," *Engineering Failure Analysis*, vol. 77, pp. 1–22, Jul. 2017.

[18] C. Trivedi, B. Gandhi, and M. J. Cervantes, "Effect of transients on Francis turbine runner life: a review," *Journal of Hydraulic Research*, vol. 51, no. 2, pp. 121–132, 2013.

[19] C. Rodriguez, E. Egusquiza, X. Escaler, Q. Liang, and F. Avellan, "Experimental investigation of added mass effects on a Francis turbine runner in still water," *Journal of Fluids and Structures*, vol. 22, no. 5, pp. 699–712, Jul. 2006.

[20] Q. Liang, C. Rodriguez, E. Egusquiza, X. Escaler, M. Farhat, and F. Avellan, "Numerical simulation of fluid added mass effect on a francis turbine runner - ScienceDirect," *Computers & Fluids*, vol. 36, no. 6, pp. 1106–1118, Jul. 2007.

[21] B. Nenneman, C. Monette, and J. Chamberland-Lauzon, "Hydrodynamic damping and stiffness prediction in Francis turbine runners using CFD," vol. 49, 2016, p. 072006.

[22] T. Theodorsen, "General Theory of Aerodynamic Instability and the Mechanism of Flutter," Tech. Rep., Jan. 1949.

[23] S. Turek, J. Hron, M. Razzaq, H. Wobker, and M. Schäfer, "Numerical benchmarking of fluid-structure interaction: A comparison of different discretization and solution approaches," in *Fluid Structure Interaction II*. Springer, 2011, pp. 413–424.

[24] T. J. Hughes, W. K. Liu, and T. K. Zimmermann, "Lagrangian-eulerian finite element formulation for incompressible viscous flows," *Computer methods in applied mechanics and engineering*, vol. 29, no. 3, pp. 329–349, 1981.

[25] M. Schäfer, M. Heck, and S. Yigit, "An implicit partitioned method for the numerical simulation of fluid-structure interaction," in *Fluid-structure interaction*. Springer, 2006, pp. 171–194.

[26] W. A. Wall, D. P. Mok, and E. Ramm, "Partitioned analysis approach of the transient coupled response of viscous fluids and flexible structures," in *Solids, structures and coupled problems in engineering, proceedings of the European conference on computational mechanics ECCM*, vol. 99, 1999, p. 182.

[27] M. Razzaq, S. Turek, J. Hron, J. Acker, F. Weichert, I. Grunwald, C. Roth, M. Wagner, and B. Romeike_, "Numerical simulation and benchmarking of fluid-structure interaction with application to hemodynamics," in *Fundamental Trends in Fluid-Structure Interaction*. World Scientific, 2010, pp. 171–199.

[28] C. M. Colciago, S. Deparis, and A. Quarteroni, "Comparisons between reduced order models and full 3d models for fluid–structure interaction problems in haemodynamics," *Journal of Computational and Applied Mathematics*, vol. 265, pp. 120–138, 2014.

[29] W. Q. Wang, X. He, L. Zhang, K. M. Liew, and Y. Guo, "Strongly coupled simulation of fluid–structure interaction in a francis hydroturbine," *International Journal for Numerical Methods in Fluids*, vol. 60, no. 5, pp. 515–538, 2009.

[30] J. Vierendeels, "Implicit coupling of partitioned fluid-structure interaction solvers using reduced-order models," in *Fluid-Structure Interaction*. Springer, 2006, pp. 1–18.

[31] M. J. Lighthill, "On displacement thickness," *Journal of Fluid Mechanics*, vol. 4, no. 4, pp. 383–392, Aug. 1958.

[32] H. J.-P. Morand and R. Ohayon, *Fluid structure interaction-Applied numerical methods*. Wiley, 1995, no. BOOK.

[33] N. Hermant, F. Chouly, F. Silva, and P. Luizard, "Numerical study of the vibrations of an elastic container filled with an inviscid fluid," *ZAMM-Journal of Applied Mathematics and Mechanics/Zeitschrift für Angewandte Mathematik und Mechanik*, vol. 98, no. 4, pp. 602–621, 2018.

[34] C. Monette, A. Coutu, and O. Velagandula, "Francis runner natural frequency and mode shape predictions," *Waterpower XV (Chattanooga, USA, 23-26 July)*, 2007.

[35] M. Á. Fernández and P. Le Tallec, "Linear stability analysis in fluid–structure interaction with transpiration. Part I: Formulation and mathematical analysis," *Computer Methods in Applied Mechanics and Engineering*, vol. 192, no. 43, pp. 4805–4835, Oct. 2003.

[36] ——, "Linear stability analysis in fluid–structure interaction with transpiration. Part II: Numerical analysis and applications," *Computer Methods in Applied Mechanics and Engineering*, vol. 192, no. 43, pp. 4837–4873, Oct. 2003.

[37] F. Hecht, "New development in freefem++," *J. Numer. Math.*, vol. 20, no. 3-4, pp. 251–265, 2012. [Online]. Available: https://freefem.org/

[38] C. Geuzaine and J.-F. Remacle, "Gmsh: A 3-d finite element mesh generator with built-in pre-and post-processing facilities," *International journal for numerical methods in engineering*, vol. 79, no. 11, pp. 1309–1331, 2009.

[39] M. Imregun and D. Ewins, "Complex modes-origins and limits," in *Proceedings-SPIE The International society for optical engineering*. SPIE INTERNATIONAL SOCIETY FOR OPTICAL, 1995, pp. 496–496.

[40] U. Fuellekrug, "Computation of real normal modes from complex eigenvectors," *Mechanical Systems and Signal Processing*, vol. 22, no. 1, pp. 57–65, Jan. 2008.

[41] M. A. Fernández, "Modèles simplifiés d'interaction fluide-structure," phdthesis, Université Paris Dauphine - Paris IX, Dec. 2001.

[42] K. Morgan, J. Periaux, and F. Thomasset, *Analysis of laminar flow over a backward facing step*. Springer, 1984.

[43] X. Hang, Q. Fei, and W. Su, "A mode tracking method in aeroelastic stability analysis using left eigenvectors," in *2018 AIAA/ASCE/AHS/ASC Structures, Structural Dynamics, and Materials Conference*, 2018, p. 1204.

[44] M. Pastor, M. Binda, and T. Harčarik, "Modal assurance criterion," *Procedia Engineering*, vol. 48, pp. 543–548, 2012.